UNIVERSITY OF BIRMINGHAM
University of Birmingham Research at Birmingham

Leader β-cells coordinate Ca^{2+} dynamics across pancreatic islets in vivo

Salem, Victoria; Delgadillo Silva, Luis; Suba, Kinga; Georgiades, Eleni; Mousavy Gharavy, S. Neda; Akhtar, Nadeem; Martin-Alonso, Aldara; Gaboriau, David C. A.; Rothery, Stephen M.; Stylianides, Theodoros; Carrat, Gaelle; Pullen, Timothy J.; Pal Singh, Sumeet; Hodson, David; Leclerc, Isabelle; Shapiro, A. M. James; Marchetti, Piero; Briant, Linford J. B.; Distaso, Walter; Ninov, Nikolay

DOI:
10.1038/s42255-019-0075-2

License:
Other (please specify with Rights Statement)

Document Version
Peer reviewed version

Citation for published version (Harvard):
Salem, V, Delgadillo Silva, L, Suba, K, Georgiades, E, Mousavy Gharavy, SN, Akhtar, N, Martin-Alonso, A, Gaboriau, DCA, Rothery, SM, Stylianides, T, Carrat, G, Pullen, TJ, Pal Singh, S, Hodson, D, Leclerc, I, I_{2+}Shapiro, AMJ, Marchetti, P, Briant, LJB, Distaso, W, Ninov, N & Rutter, GA 2019, 'Leader β-cells coordinate Ca^{2+} dynamics across pancreatic islets in vivo', *Nature*, vol. 1, no. 6, pp. 615-629. https://doi.org/10.1038/s42255-019-0075-2

Link to publication on Research at Birmingham portal

Publisher Rights Statement:
This is the accepted version of the following article: Salem, V, Delgadillo Silva, L, Suba, K, Georgiades, E, Mousavy Gharavy, SN, Akhtar, N, Martin-Alonso, A, Gaboriau, DCA, Rothery, SM, Stylianides, T, Carrat, G, Pullen, TJ, Pal Singh, S, Hodson, D, Leclerc, I, Shapiro, AMJ, Marchetti, P, Briant, LJB, Distaso, W, Ninov, N & Rutter, GA. (2019) 'Leader -cells coordinate Ca2+ dynamics across pancreatic islets in vivo', Nature, vol. 1, pp. 615-629, which has been published in final form at https://doi.org/10.1038/s42255-019-0075- 2

General rights
Unless a licence is specified above, all rights (including copyright and moral rights) in this document are retained by the authors and/or the copyright holders. The express permission of the copyright holder must be obtained for any use of this material other than for purposes permitted by law.

•Users may freely distribute the URL that is used to identify this publication.
•Users may download and/or print one copy of the publication from the University of Birmingham research portal for the purpose of private study or non-commercial research.
•User may use extracts from the document in line with the concept of 'fair dealing' under the Copyright, Designs and Patents Act 1988 (?)
•Users may not further distribute the material nor use it for the purposes of commercial gain.

Where a licence is displayed above, please note the terms and conditions of the licence govern your use of this document.

When citing, please reference the published version.

Take down policy
While the University of Birmingham exercises care and attention in making items available there are rare occasions when an item has been uploaded in error or has been deemed to be commercially or otherwise sensitive.

If you believe that this is the case for this document, please contact UBIRA@lists.bham.ac.uk providing details and we will remove access to the work immediately and investigate.

Download date: 19. Apr. 2024

Leader β cells coordinate Ca^{2+} dynamics across pancreatic islets *in vivo*

Victoria Salem[1,†*], Luis Delgadillo Silva[2†], Kinga Suba[1], Eleni Georgiadou[1], S. Neda Mousavy Gharavy[1], Nadeem Akhtar[2], Aldara Martin-Alonso[1], David C.A. Gaboriau[4], Stephen M. Rothery[4], Theodoros Stylianides[3], Gaelle Carrat[1], Timothy J. Pullen[5], Sumeet Pal Singh[2], David J. Hodson[6,7], Isabelle Leclerc[1], A.M. James Shapiro[8], Piero Marchetti[9], Linford J.B. Briant[10], Walter Distaso[11], Nikolay Ninov[2,12*] and Guy A. Rutter[1*]

[1]Department of Medicine, Imperial College London, London, UK, [2]DFG-Center for Regenerative Therapies, Technische Universität Dresden, Dresden, Germany, [3]Loughborough University, Loughborough, UK, [4]FILM, Imperial College London, London, UK, [5]Department of Diabetes, Faculty of Life Science and Medicine, King's College London, London, UK,[6]Institute of Metabolism and Systems Research (IMSR), University of Birmingham, Edgbaston, UK, [7]Centre for Endocrinology, Diabetes and Metabolism, Birmingham Health Partners, Birmingham, UK; and COMPARE University of Birmingham and University of Nottingham Midlands, [8] Clinical Islet Laboratory and Clinical Islet Transplant Program, University of Alberta, Edmonton, Alberta, Canada, [9]University of Pisa, Pisa, Italy, [10]Radcliffe Department of Medicine, University of Oxford, Oxford, UK. [11]Imperial College London, UK, [12]Paul Langerhans Institute Dresden of the Helmholtz Center Munich at the University Hospital Carl Gustav Carus of TU Dresden, German Center for Diabetes Research.

[†]Equal contributions

*Corresponding authors: g.rutter@imperial.ac.uk; v.salem@imperial.ac.uk; nikolay.ninov@tu-dresden.de

ABSTRACT

Pancreatic β cells form highly connected networks within isolated islets. Whether this behaviour pertains *in vivo*, after innervation and during continuous perfusion with blood, is unclear. Here, we use the recombinant Ca^{2+} sensor GCaMP6 to assess glucose-regulated connectivity in living zebrafish *D. rerio,* and in murine or human islets transplanted into the anterior eye chamber. In each setting, Ca^{2+} waves emanated from temporally-defined leader β cells and 3D connectivity across the islet increased with glucose stimulation. Photo-ablation of zebrafish leader cells disrupted pan-islet signalling, identifying these as likely pacemakers. Correspondingly, in engrafted mouse islets, connectivity was sustained during prolonged glucose exposure, and super-connected "hub" cells were identified. Granger causality analysis revealed a controlling role for temporally-defined leaders, and transcriptomic analyses a discrete hub cell fingerprint. We thus define a population of regulatory β cells within coordinated islet networks *in vivo*. This population may drive Ca^{2+} dynamics and pulsatile insulin secretion.

WORDS: 150

Keywords: Pancreatic islet, zebrafish, functional imaging, Ca^{2+} dynamics, GCaMP6, β cell, in vivo, connectivity, photo-ablation, transcriptomics, cluster analysis, Granger causality.

BACKGROUND.

Defective insulin secretion underlies diabetes mellitus, a disease affecting almost 1 in 8 of the adult population worldwide, consuming 10 % of healthcare budgets of westernized societies (https://www.idf.org/). Impaired secretion is absolute in type 1 diabetes and relative in type 2 diabetes [1].

Individual β cells within the pancreatic islets possess all of the enzymatic machinery required for glucose sensing and insulin secretion [2, 3], although marked heterogeneity exists at the transcriptomic [4, 5, 6, 7], metabolic [8], electrophysiological [9, 10] and secretory [11-13] levels. Questions remain over whether this heterogeneity has any functional significance, and could, for example, contribute to the pulsatile release of insulin [14].

Connections between individual β cells [15, 16] are essential for the normal control of hormone secretion [10, 14, 17]. Using Ca^{2+} imaging of isolated islets *in vitro* two distinct, but complementary, ways of analysing β cell connectivity have emerged. Earlier studies described an increase in the number of correlated cell pairs using Pearson-based analysis, which assesses similarities between the Ca^{2+} traces for individual cells over time [18, 19]. This strategy revealed that stimulation with glucose or glucagon like peptide-1 causes pan-islet increases in β cell connectivity which are disrupted under conditions mimicking type 2 diabetes (e.g. “gluco(lipo)toxicity”). More recently, we have applied an approach based on signal binarization [20] and reported that a subset of 5-8 % β cells form super-connected “hubs” within the interconnected network [18]. We also demonstrated that these cells are likely to serve as pacemakers [21]. Both of these approaches utilise the term “connectivity” to describe the functional coactivity of β cells within an islet.

The behaviour of the isolated islet in culture [18, 21] is likely to differ significantly from that *in vivo* where islets are continuously perfused with blood and receive complex neural inputs. Imaging of the islet within the intact pancreas *in vivo* is, however, challenging and requires exteriorisation of the whole organ. A powerful alternative approach is the engraftment of islets into the anterior eye chamber [22]. Combined with the use of stably-expressed, recombinant fluorescent probes [23, 24] this creates an optically-accessible platform allowing repeated measurements over time if required [25]. Here, we use this strategy, alongside an analogous genetic modification of the zebrafish [26] to record multilayer β cell Ca^{2+} dynamics in the intact living animal [27]. Pancreatic islets display a largely conserved size, but partly species-specific [28] arrangement of neuroendocrine cell types [29], important for the proper control of insulin secretion [17]. In the zebrafish, most of the pancreatic endocrine cells are located in a single primary islet [27]. By 5 days post fertilization (dpf) (as used in these

experiments) zebrafish larvae have developed a primary islet which contains an average of 30 β cells that express mature markers like Ucn3l [26]. Later in the juvenile stage, the zebrafish still possesses the large, embryonically-derived primary islet and has also developed many smaller secondary islets [30]. We have previously shown that the primary zebrafish islet responds *in vitro* to glucose [26] and ablation of β cells at this developmental stage leads to glucose intolerance in the larva [31]. Thus, by 5 dpf the primary islet is glucose responsive and systemically connected, serving as an excellent model to study islet β cell coordination.

We demonstrate that glucose induces strongly co-ordinated pan-islet Ca^{2+} responses in each setting, with a definable point of origin and propagation characteristics in three dimensions. In zebrafish, the ablation of "leader" cells, i.e. those which respond first to glucose challenge, results in a dampening of the response of the islet to subsequent stimulation with glucose, redolent to the effects of optogenetic inactivation of "hub" cells in the isolated mouse islet [21]. In the mouse, analyses based on signal binarization and Monte Carlo-like shuffling/randomisation [21] demonstrate the existence of a population of super-connected cells under stimulatory conditions *in vivo*. Moreover, causality analysis [32, 33] unites these observations in fish and mouse by demonstrating that temporally-defined "leader cells" are also those that were causally the most closely linked to other β cells, whilst analyses of single cell RNASeq data suggests they may possess a unique transcriptional profile. Hence, we demonstrate that a functional β cell hierarchy exists *in vivo*, and may control pulsatile insulin secretion.

METHODS

Zebrafish husbandry.

Zebrafish wild type (WT) AB, WIK and TL were used in all the experiments. Zebrafish were raised in standard conditions at 28 °C. Established transgenic lines used in this study were *Tg(ins:gCaMP6s;cryaa:mCherry)* [26], *Tg(ins:cdt1-mCherry;cryaa:GFP)* [31] and *Tg(gata1a:DsRed)* [26]. *Tg(ins:cdt1-mCherry)* was utilised in preference of a pan β cell marker such as *Tg(ins:mKO-nls)* to allow for a clear separation of the spectra and simultaneous signal recordings from the GCaMP and mCherry channels, which was particularly important during fast imaging. All experiments were carried out in compliance with European Union and German laws (Tierschutzgesetz) and with the approval of the TU Dresden and the Landesdirektion Sachsen Ethics Committees (approval number: AZ 24D-9168,11-1/2013-14, TV38/2015, T12/2016, and T13/2016, TVV50/2017, and TVV 45/2018)). All live imaging *in vivo*, compound and glucose-injections, as well as experimental procedures were performed with zebrafish larvae that did not exceed five days post fertilization (dpf), as stated in the animal protection law (TierSchVersV §14). *Ex vivo* live-imaging of beta-cells was performed with isolated islets from euthanized fish according to approval T12/2016.

Zebrafish glucose measurements.

Groups of ten larvae were pooled together, snap frozen in liquid nitrogen, and then stored at -80°C. Following thawing on ice, 250 µL of PBS were added and the larvae were sonicated with an ultrasonic homogenizer (Bandelin, SONOPLUS), prior to centrifugation at 13,000g. Glucose concentration was determined using the BioVision Glucose Assay Kit (Biovision Inc, California, US) according to the manufacturer's instructions.

Intra-cardiac injection in zebrafish.

Injections were performed using pulled glass pipettes with a 5nL tip volume calibrated microscopically (3.5'' Drummond #3-000-203-G/X, Sutter pipette puller P-1000). A pneumatic pico-pump (FemtoJet, Eppendorf), injecting pressure 500 hPa and compensation pressure of 0 hPa, was used to deliver a 1 second injection into the pericardial cavity in the agarose-mounted larva, assisted by a micromanipulator (InjectMan N2, Eppendorf). Doses were 5 nL of 25 mM glucose and 5 nL insulin at 100 units/ml.

Zebrafish live imaging.

Embryos were treated with 0.003% (200 µM) 1-phenyl 2-thiourea (PTU) to inhibit pigmentation from 1 dpf onwards. At 4.5 dpf, the larvae were anaesthetized using 0.4g/L

Tricaine. The larvae were mounted in glass-bottomed microwell dishes (MatTek corporation) using 1% low-melting agarose containing 0.4g/L Tricaine. After the agarose was solidified, the dishes were filled with embryonic fish water and 0.4g/L Tricaine. Live imaging was performed on an inverted laser scanning confocal system ZEISS LSM 780 inverted with a C-Apochromat 40X/N.A. 1.2 water correction lens. In the *Tg(ins:GCaMP6s);Tg(ins:cdt1-mCherry)* double-transgenic animals, we acquired the GCaMP6s and mCherry signals simultaneously using the 488nm and 561nm laser lines. The GCaMP6s signal was rendered in green and the nuclear signal in red. Videos were recorded at a 10 s/image (0.1 Hz) frame rate unless indicated otherwise, with a Z-step thickness of 1.2 µm, covering on average 35 µm, and an XY resolution of 0.12 µm per pixel (512x512 pixels). Laser power was maintained as low as possible (<1.5%) to minimise phototoxicity. For faster imaging, we focused on a single plane, recording a frame every 300 milliseconds with an XY resolution of 0.08 µm per pixel (512x512 pixels).

Zebrafish fast whole islet live imaging.

Whole islet live-imaging at an acquisition rate of 0.8Hz, covering ~700µm^3, was achieved using resonant scanner technology with an inverted laser scanning confocal system (Leica SP5 MP) using an IRAPO L 25X/N.A. 0.95 water lens. Videos were recorded at ~0.8 Hz per Z-stack (~700µm^3), with a Z-step thickness of 4.5 µm, covering on average 70 µm in depth, and an XY resolution of 0.24 µm per pixel (256x256 pixels). The resonant scanner was set at 8,000 Hz with a bidirectional line scanning in order to achieve maximum speed.

Selective two-photon laser ablation of leader cells.

Live imaging and intra-cardiac glucose injections were performed as described above using *Tg(ins:gCaMP6s;cryaa:mCherry), Tg(ins:cdt1-mCherry;cryaa:GFP)* larvae. Images were captured across a single confocal plane at an imaging acquisition rate of six frames/second (6Hz). We performed three independent injections of glucose, separated by 5 min. intervals. The “leader cell” (that is the temporally-defined first responder) was identified by eye based on the changes in GCaMP6s-fluorescence after each glucose-injection. The larvae were then transferred to a Leica SP5 MP confocal microscope, equipped with a two-photon laser and 25X/0.95 N.A objective. A region of interest (ROI) was selected encompassing the center of the nucleus of the cell to be ablated, covering a circle with an approximate diameter of 0.5 µm. The cell of interest was then exposed to two-photon laser irradiation at the output power of 2.0 W ($\lambda = 800$ nm) for 5 s to minimize possible damage to other areas. We then performed live imaging and intra-cardiac injection again, using the protocol above, and within 20 min. of irradiation, to record the response following cell ablation. Control cells

that were not the temporally-defined first responders ("followers") were ablated with the same methodology as leader cells. To ensure that the laser ablation technique was highly localised to a single cell, as expected with this approach, we fixed islets immediately after the laser cell-ablation (<10 min) then labelled them with insulin antibody and DAPI (see below).

Islet blood flow imaging in zebrafish.

Imaging of islet blood flow was performed using triple transgenic larvae *Tg(ins:GCaMP6s);Tg(ins:cdt1-mCherry);Tg(gata1a:DsRed).* *Tg(gata1a:DsRed)* reporter was used as a marker of red blood cells. Live imaging was performed on a ZEISS LSM 780 confocal microscope equipped with a C-Apochromat 40X/1.2 NA water correction lens. The GCaMP6s and mCherry signals from β cells, and DsRed signals from blood cells, were simultaneously acquired using the 488nm and 561nm laser lines. The GCaMP6s signal was rendered in green. The blood cells and the nuclear signal of β cells were rendered in red. We focused on a single plane and the videos were recorded at a frame rate of 1 frame/155 milliseconds (~6.4 Hz).

Mechanical heart stop in zebrafish.

To stop the blood flow in zebrafish larvae, a glass-pulled pipette (3.5'' Drummond #3-000-203-G/X, Sutter pipette puller P-1000), with a manually blunted end, was used to exert a direct pressure into the heart. The heart was blocked for around 400 s. The mechanical heart stopping was executed during live Ca^{2+} imaging in the *Tg(ins:GCaMP6s);Tg(ins:cdt1-mCherry)* double-transgenic larvae, as described above. Videos were recorded at a 10 s frame rate (0.1 Hz), and a Z-step thickness of 2.8 µm, covering on average 50 µm, with a frame size of 512 x 512 pixels.

Identification of dorsal- and ventral-bud derived β cells.

The primary zebrafish islet contains both dorsal bud-derived β cells (DBCs) and ventral bud-derived β cells (VBCs). To interrogate whether embryonic derivation affected the identity of leader cells, we performed injection of mRNA encoding H2B-RFP to distinguish between D- and VBCs based on label dilution [34]. In this assay, DBCs retain the H2B-RFP label whereas VBCs dilute it. We injected one-cell stage embryos with mRNA expressing H2B-mCherry. We maxi-prepped the pCS2+H2B-mCherry plasmid, digested it with KpnI and in vitro transcribed it using the SP6 Transcription Kit (Ambion, AM1340) to generate mRNA. We injected 100pg of H2B-mCherry mRNA in each embryo. Larvae were mounted as described above for whole islet live imaging and glucose-injections.

Post mortem staining for cell ablation in zebrafish.

After the live imaging was performed, and the leader cells were temporally identified, the larvae were immediately fixed in 4% PFA overnight. Then the samples were permeabilized with 1% PBT (Triton-X-100) for 1hr. To avoid non-specific primary antibody binding, we blocked for 2hrs in PBTB (PBT + 4% BSA). Nuclear staining was performed using DAPI at 1:1000 dilution. After the immunostaining with anti-insulin (polyclonal guinea pig anti-Insulin, Dako A0564, 1:300 dilution), the samples were mounted in Vectashield. The anti-insulin antibody has been previously validated to mark β-cells in zebrafish by us using transgenic lines that express GFP under the insulin promoter and was also recently validated to show negative immunoreactivity in β-cells in homozygous mutant fish for the *insulina* gene (PMID: 30520733), confirming its high specificity. Images were acquired using Z-Stacks on a LSM-780 Zeiss confocal microscope. For image analysis, the nuclei of the β cells were segmented using the DAPI channel.

Ex vivo imaging of primary and secondary zebrafish islets.

The islet culture and imaging were performed as previously described [35]. Primary and secondary islets were isolated from three month post fertilization (mpf) *Tg(ins:gCaMP6s; cryaa:mCherry)* animals. The islets were stimulated with a ramp of 10 and 20 mM D-glucose (Sigma, G8270). The imaging culminated with the addition of 30mM KCl (Sigma, P9451) in the same plate. Videos were recorded at a 2.5 s/image (0.25 Hz frame rate), in a single Z-plane and with an XY resolution of 0.59 µm per pixel (1024x1024 pixels). After imaging, individual β cell ROIs were manually drawn using Image J. Fluorescence intensity (FI) was normalized using the minimum and maximum values of FI across frames for each cell. Cells which did not show an increase in GCaMP signal after KCl addition, were not included in the analysis.

Image analysis from in vivo imaging of zebrafish.

The cumulative population response of β cells was quantified from maximum intensity projections (MIP) of the z-stack. In the MIP, the islet area was delimited manually using the Region of Interest (ROI) Manager in ImageJ (https://imagej.net/Fiji) [36]. Using the ROI, the integrated fluorescence intensity of GCaMP6s was extracted. The integrated fluorescence intensity was normalized for the whole imaging time using the following formula:

$(F_T – F_{MIN}) / (F_{MAX} – F_{MIN})$,

where F_T is the integrated fluorescence intensity at a given time while F_{MAX} and the F_{MIN} are the maximum and minimum values recorded during the live imaging session, respectively.

Single-cell signal analysis of GCaMP signal was performed either from single-confocal slices covering a majority of imaged β cells (2D) or by segmenting the nuclei from the Z-stacks using the nuclear mCherry signal (3D). For nuclear segmentation, we utilized the 3D image suite in Image J, and the 3D iterative thresholding plugin [37]. The following parameters were set based on the estimated approximate nuclear size of β cells: minimum volume = 100 pixels; maximum volume = 1200 pixels; criteria method = "volume"; threshold method = "volume"; value method = 10 units. This generated a voxel covering the nuclei of β cells. Using the 3D ROI manager plugin, we extracted the integrated fluorescence intensity from each voxel over time (FT). In order to create 3D plots, we first extracted the centroids from each voxel and then plotted them using the R software and the package "rgl". Single-cell heat-maps based on 2D analysis were created using Excel and conditional formatting setting the colors in a gradient from 0 to 1. For visualization, the brightness and contrast was adjusted uniformly across the times series using ImageJ, and the tool Brightness/Contrast.

Quantification of GCaMP6s fluorescence intensity in zebrafish images.

For the quantification of changes in GCaMP6 fluorescence upon glucose or insulin injection in Figure 1 and Supplementary Figure 1, the cumulative response of all imaged β-cells to glucose injection was quantified. To this end, we compared the area under the curve based on the normalized integrated fluorescence intensity 10 frames before and after the injections of glucose or insulin (covering 200 seconds of imaging) using the formula:

$$(F_T – F_{MIN}) / (F_{MAX} – F_{MIN}),$$

For the quantification of changes in GCaMP6 fluorescence upon laser-cell ablation (Figure 4), the cumulative response of all imaged β cells to glucose injection was quantified. In this case, the maximum value (F_{MAX}) was not used for normalization since such normalization could mask the effect of loss of response following cell ablation due to normalization to background fluorescence. Instead, we only subtracted the background from the imaging session using the following formula:

$$(F_T – F_{MIN}) / F_{MIN}$$

The larvae were injected with three separate pulses of glucose before and after the ablation. For each injection the GCaMP area under the curve was calculated covering 200 frames

after the glucose injection. The average area under the curve was calculated before and after the ablation and plotted as $\log_2$.

Spatial drift correction OF ZEBRAFISH images.

The red channel (cdt1-mCherry) signal from the β cell nuclei was used to correct for spatial drift in the green GCaMP6s channel. A maximum projection of each Z-stack in the time series was entered into the FIJI plugin "Descriptor-based series registration (2d/3d + t)" (https://imagej.net/Descriptor-based_registration (2d/3d))[38], applying the model "Rigid (2d)", with "3-dimensional quadratic fit". A sigma of 13 and threshold of 0.03 was applied to the detection of nuclear signal, with a minimum number of three neighbors, redundancy of 1 and a random sample consensus (Ransac) error of 5. Matching across time series was achieved using global optimization, unless indicated otherwise. Stabilization in the Z dimension was achieved using the Fiji "Reslice" command. The "Descriptor-based series registration (2d/3d + t)" plugin was used with nuclei detection sigma set to 5 and with a threshold of 0.03.

Mouse husbandry.

Male C57Bl/6 wild type (WT) (18-25g) mice were purchased from Charles River, UK, and used as donor islet recipients. For *in vivo* measurements of cytosolic Ca^{2+} in pancreatic β cells, we generated mice that express GCaMP6f in β cells using the Cre-Lox system. Briefly, we crossed Ins1Cre mice (provided by J Ferrer, this Department) [39, 40] with mice that express GCaMP6f downstream of a *Lox*P-flanked STOP cassette (The Jackson Laboratory, stock no. 028865). Islets donated from either sex were used for transplantation. Mice were housed in groups of six in individually-ventilated cages under controlled conditions (21-23°C; 12 h light: 12 h dark cycle). Male BALBc *nu/nu* (The Jackson Laboratory, stock no. 002019) recipients were used for human islet transplantation. Animals had *ad libitum* access to standard chow and water (irradiated for the immunocompetent mice). All animal procedures were approved and performed under the UK Home Office Animals (Scientific Procedures) Act 1986 (Project License to I.L., PA03F7F07 at Imperial College London. The project licence received internal institutional ethical approval as well as external Home Office approval).

Generation of adenovirus expressing GCaMP6m (AV-GCaMP6m).

A plasmid driving the expression of *GCaMP6m* under the control of the cytomegalovirus (CMV) promoter (CMV-AVGCaMP6m) was generated using the pAdEasy system [41]. Briefly, pGP-CMV-GCaMP6m plasmid (Addgene plasmid # 40754) was digested using *Bgl*II and

*Not*I. The released GCaMP6m fragment was then purified and ligated into pShuttle-CMV vector (Addgene plasmid # 16403). CMV-GCaMP6m was inserted by recombination into the adenoviral pAdEasy-1 vector (Addgene plasmid # 16400), and transformed into electrocompetent BJ5183 cells. The isolated plasmid was subsequently amplified in reduced recombination rate (recA1) NEB-10β competent *E. coli* (New England BioLabs). Following the transfection of AD293 cells with the linearized pAdEasy-CMV-GCaMP6m construct, cells were harvested and lysed to release virions. The virus was further amplified and purified by centrifugation on a CsCl gradient. Titration was performed by infecting AD293 cells with serially diluted viral stocks, counting positive cells through GCaMP6m fluorescence.

Islet transplantation into murine anterior chamber of the eye (ACE).

Pancreatic islets were isolated and cultured as described previously [42]. For transplantation, 10-20 islets were aspirated with a 27-gauge blunt eye cannula (BeaverVisitec, UK) connected to a 100ul Hamilton syringe (Hamilton) via 0.4-mm polyethylene tubing (Portex Limited). Prior to surgery, mice were anaesthetised with 2-4% isoflurane (Zoetis) and placed in a stereotactic frame to stabilise the head. The cornea was incised near the junction with the sclera, being careful not to damage the iris. Then, the blunt cannula, pre-loaded with islets, was inserted into the ACE and islets were expelled (average injection volume 20 µl for 10 islets). Carprofen (Bayer, UK) and eye ointment were administered post-surgery.

In vivo Ca^{2+} imaging of AV-GCaMP6m infected murine islets in the ACE.

Prior to transplantation into the ACE of recipients, isolated islets (from WT C57/BL6 donors, <24 weeks old or human islet donations) were infected with AV-GCaMP6m *in vitro* at a multiplicity of infection (MOI) of 20 for 24 h. This approach, which was expected to allow the identification, if present, of functional islet sub-compartments (i.e. local groups of interacting β cells) provided preferential infection of superficial β cells (1-2 cells deep). Of these, ~ 50 % were infected. A minimum of four weeks was allowed for full implantation of transplanted islets before imaging. Imaging sessions were performed with the mouse held in a stereotactic frame and the eye gently retracted, with the animal maintained under 2-4% isoflurane anaesthesia. All imaging experiments were conducted using a spinning disk confocal microscope (Nikon Eclipse Ti, Crest spinning disk, 20x water dipping 1.0 NA objective). The signal from AV-GCaMP6m fluorophore (ex. 488 nm, em. 525±25 nm) was monitored in time-series experiments for up to 20 min. at a rate of 1 frame/sec. Ca^{2+} traces were recorded for three min. prior to intraperitoneal (IP) glucose injection, with a mean blood glucose reading (across five islets in five separate animals) of 8 mmol/L. Three minutes into acquisitions mice received 150 µl 30% (1.5g/kg) bolus of glucose intra-peritoneally (IP). Blood glucose was subsequently measured on a glucometer (Accu-Chek, UK) at two-minute

intervals from a tail vein nick until the end of experiments. Injection of glucose at 180 s raised blood glucose to an average of 28 mM for the remainder of the 10 min. imaging series. Since the mouse imaging experiments are the first of their kind, sample size (n=5 islets in n= 5 animals) was determined to be adequate based on the magnitude and consistency of measurable differences between groups. This was in line with other studies examining islets in the ACE [22].

In vivo Ca^{2+} imaging of Ins1Cre-GCaMPf islets in the ACE.

Ins1Cre-GCaMP6f (ex.: 488nm, em. 525±25 nm) -expressing islets were isolated and transplanted into WT recipients (*n*=5 islets in *n*=5 different animals), and imaged as described above. Stream acquisitions of a single x/y plane of β cells recorded 2 min. datasets at 3Hz. Islets (*n*=5 islets in *n*=5 different animals) were continuously monitored and the focus was manually adjusted to counteract movement. Islets (in the same imaging session) were imaged under both “low glucose” (2–6 mM) and “high glucose” (17-25 mM) conditions (randomly ordered). Blood glucose (tail nick, Accu-chek glucometer) was assessed at 2 min. intervals throughout. Low glucose readings were obtained following the intravenous (IV) administration of insulin (Actrapid, 0.3ml of 1.0 iu/ml), and high glucose was achieved with a 200 µl 30% (2g/kg) IP bolus of sugar. At the end of experiments animals were allowed to recover and were further monitored for an hour for potential post-operative latent hypoglycaemia.

To extend the image acquisitions to collect 3-dimensional data (ie. three separate planes of β cells across an islet), a piezo device was attached to the inverted objective. This allowed for rapid, precise, 15 µm z-movements such that a 3-slice z-stack could be obtained at a whole-islet imaging rate of 1 fps. At this imaging speed, we were able to obtain 3D connectivity readouts for low and high glucose conditions (as described above, *n*=3 islets in *n*=3 different animals). As we became more expert with the ability of our platform, this number of experiments was sufficiently powered to demonstrate the rise in connectivity from low to high glucose in the 3D imaging experiments,

Finally, we examined islet Ca^{2+} dynamics during a longer period of glucose stimulation, to exclude the possibility that pan-islet connectivity is related to spatially aggregated β cells simply responding acutely and synchronously to a rise in circulating glucose concentration. Five animals (five separate islets studied, in line with former acute experiments) were placed under isofluorane anaesthesia for 60 minutes. At the start of the imaging session an IP bolus of sugar was administered. This led to a slow and sustained rise in circulating blood

sugar (measured every 3-5 minutes via tail vein sampling, as before). 30-50 minutes into this imaging session, a 10-minute single plane islet recording was taken at 1fps, manually readjusted in real time for movement. This was performed at "high" glucose levels (i.e. when blood sugar levels had risen after IP glucose injection to a high, steady level >12 mmol/L). We also report connectivity at a previous stage in the imaging session (10-20 minutes in) when circulating glucose levels were at an intermediate (medium glucose, 7-10 mmol/L) range (but the islets were still exhibiting coordinated wave activity). In the same imaging session, the islets were recorded following IV administration of insulin when circulating levels of glucose were low (< 4 mmol/L). The same islet plane and β cell ROIs were investigated under each of the three (low, medium and high) circulating glucose conditions. To ensure that the findings from this experiment were unaltered with the use of another anaesthetic, we repeated these experiments using ketamine (Zoetis) and xylazine (Bayer) (90 mg/kg and 4.5 mg/kg cocktail respectively), with similar findings.

In vivo Ca^{2+} imaging of AV-GCaMP6m infected human islets

We studied the behaviour of 11 individual human islets (four individual donors, age range 14-74 years, non-diabetic, BMI range 21.5 to 29.2; see Supplementary Figure 5) that had been transduced with AV-GCaMP6m and transplanted into the ACE of (immunocompromised) BALB/c *nu/nu* mice. A human donor with diabetes (female, 54 years old, BMI 24.4, type 2 diabetic for 10 years, insulin dependent for the last 1.5 yrs) provided islets for two experiments (separate islets in separate BALB/c *nu/nu* recipients). Human islets were obtained from multiple institutions (co-authors AMJS at the University of Alberta, Edmonton, Canada and PM at the University of Pisa, Italy). Permission for the use of human tissue was provided at Imperial College by the Charing Cross Research Ethics Committee, REC reference number 07/H0711/114. Human islets were obtained post mortem with next of kin and local and ethical permission at the sites of procurement. There was no selection procedure for the implantation of human donor islets, and they were implanted into recipient mice as they became available. Donor data are fully anonymised and no clinical data beyond age, gender, and cause of death were available.

Following an imaging protocol described for the Ins1Cre-GCaMP6f mouse studies above, we measured human islet behaviour under imposed low (< 4 mM) and high (>7 mM) glucose conditions. Since BALB/c mice are resistant to glucose rises under anaesthesia, there are more successful imaging results in the low glucose state reported. *Image analysis.* Using FIJI (Image J) software (see above), images in the time series were individually time stamped, to maintain their absolute time information, before excluding frames where resolution was poor or blurred by movement. Image series were then cropped and manually

aligned across all frames using a pre-defined region of interest (ROI) as reference. Creating ROIs for analysis was guided by the emitted GCaMP fluorescence and the negative shadow of nuclei. For the virally infected islets each ROI extended over the entirety of a cell, whereas ROIs in experiments with transgenic islets covered sub-cellular regions in close proximity to nuclei. Mean fluorescence intensity and XY(Z) co-ordinates for each cell within an islet (ROIs) were compiled and processed for connectivity analysis.

Pearson (R)-based connectivity analyses.

Correlation analyses between the Ca^{2+} signal time series for all cell pairs in an imaged islet were performed in MATLAB using a custom-made script (available upon request). Data were smoothed using a retrospective averaging method (previous 10 values) and all traces were normalised to F0. Two-sided averaging techniques were not applied as this would have invalidated subsequent causality analyses. The correlation function R between all possible (smoothed) cell pair combinations (excluding the autocorrelation) was assessed using Pearson's correlation. Data are displayed as heatmap matrices, indicating individual cell pair connections on each axes (min. = -1; max. = 1). Given that data were not normally distributed (and hence resorting to either asymptotic p-values or Monte Carlo based ones would not be useful), the data were subsequently subjected to a bootstrap resampling to increase the accuracy of the confidence interval of the R statistic, and $p<0.001$ was deemed a statistically significant cell-cell connection. The Cartesian co-ordinates of the imaged cells were then taken into account in the construction of connectivity line maps. Cell pairs ($R>0.25$ AND $p<0.001$ post bootstrap) were connected with a straight line, the colour of which represented the correlation strength and was assigned to a colour-coded light-dark ramp (R=0.25-0.5 [green], R=0.5-0.75 [yellow], R=0.75-1.0 [red]). An average coefficient of positive connectivity was computed for each condition, by averaging the positive R values (excluding the auto-correlated cells) and the percentage of cells that were significantly connected to one another was elicited, for the purposes of group comparisons.

We have not examined the immediate upstroke of an acute IV bolus of glucose i.e. from a low to a high glucose setting. Consequently the "first responders" in the mouse datasets refer to the first β cells observed to fire in a train of calcium waves during a period of more prolonged elevated glucose.

Signal binarization and Monte Carlo analysis.

To investigate what happens in the tail of the distribution, and go beyond the analysis of linear association provided by the Pearson correlation coefficient, we also looked at association between activity regimes. This analysis was performed as described previously

[20, 21]. In brief, cells were considered to be either “on” or “off” if the fluorescent signal exceeded a 20% noise threshold above baseline. Binarized data for each cell pair were assessed for co-synchronicity using the co-activity statistic $C_{ij} = T_{ij}/(\sqrt{[T_i.T_j]})$ where C is a co-activity coefficient (0 to +1), T_i and T_j represent the time spent in the active state for each given cell and T_{ij} represents the time during which both cells are active. Pairs were considered linked if their statistic displayed a higher than chance ($p<0.01$) probability of interaction *versus* a Monte Carlo permutated version of the binarized matrix dataset. A probability distribution function of these connections (pooled across five islets) was presented as a log-log plot to look for a power law relationship, the strength of which was quantified by the coefficient of determination (R^2) [38].

Granger analysis.

The mouse Ins1*Cre* GCaMP6f-expressing islet series were subjected to a Granger Causality analysis [32, 33]. Individual cell-cell pairs were separately analysed (time lag 1-3 secs, $p<0.001$) with a Bonferroni multiple comparison test. Granger-defined leaders, i.e. those cells with the greatest number of causally-linked followers, were compared with the temporally-defined leaders whose firing (in the high glucose condition) preceded the remainder of the β cell population. Granger leaders that persisted when the low, medium and high glucose experiments were performed on the same network of β cells were spatially located on the islet map to understand their spatial distribution.

Zebrafish transcriptomic analysis (single cell RNAseq).

For single-cell RNA-Seq of the zebrafish pancreatic cells using the 10x Genomics platform, cell suspension was prepared from primary islets of six 2 mpf *Tg(ins:BB1.0L)* [26] using the protocol described in [43] (*n*=6 animals). The cell suspension was passed over a 30 µm cell filter (Miltenyi Biotec, 130-041-407) to remove debris and cell-aggregates, adjusted with HBSS (without Ca, Mg) to a density of 800 cells/µl, and diluted with nuclease free water according to the manufacturer’s instructions to yield 5000 cells. Subsequently, the cells were carefully mixed with reverse transcription mix before loading the cells on the 10X Genomics Chromium system [44]. After the gel emulsion bead suspension underwent the reverse transcription reaction, emulsion was broken and DNA purified using Silane beads. The cDNA was amplified with 10 cycles, following the guidelines of the 10x Genomics user manual. The 10X Genomics single cell RNA-seq library preparation – involving fragmentation, dA-Tailing, adapter ligation and indexing PCR – was performed based on the manufacturer’s protocol. After quantification, the libraries were sequenced on an Illumina NextSeq 550 machine using

a HighOutput flowcell in paired-end mode (R1: 26 cycles; I1: 8 cycles; R2: 57 cycles), thus generating ~45 mio fragments. The raw sequencing data was then processed with the 'count' command of the Cell Ranger software (v2.1.0) provided by 10X Genomics with the option '--expect-cells' set to 5000 (all other options were used as per default). This yielded 2625 cells. To build the reference for Cell Ranger, zebrafish genome (GRCz10) as well as gene annotation (Ensembl 87) were downloaded from Ensembl and the annotation was filtered with the 'mkgtf' command of Cell Ranger (options: '--attribute=gene_biotype:protein_coding --attribute=gene_biotype:lincRNA –attribute=gene_biotype:antisense'). Genome sequence and filtered annotation were then used as input to the 'mkref' command of Cell Ranger to build the appropriate Cellranger Reference. Data are deposited at the GEO repository with an accession number GSE123662.

Cluster analysis.

scRNA-Seq data from C57BL/6 mouse islets were downloaded from NCBI GEO (GSE84133) [45]. UMI-filtered counts were analysed using the Seurat package [46]. The data were filtered and normalised then highly variable genes identified for PCA analysis and graph-based clustering. In the mouse data, insulin, glucagon and somatostatin cells were largely separated into distinct clusters. The initial clustering of the fish data produced a single cluster containing cells expressing *ins*, *gcga* and *sst1.1* (listed by ENSEMBL as the zebrafish orthologue of the H. sapiens SST gene; similar data were obtained using the *sst1.2* gene). This 'endocrine' cluster was separated from the other cells and re-clustered, producing distinct clusters for these three genes. The *ins*+ clusters were combined and the few remaining cells positive for *gcga, sst1.1 or gip*, or negative for *ins*, were excluded. Within this group of β cells, the intersection between the upper quartile of *gck* expression and lower quartile of *ins* expression was identified as putative hub cells, based on the properties of these cells described previously [21]. Genes differentially expressed between the putative hub cells and remaining β cells were identified using Wilcoxon rank sum test and the upregulated genes thus identified were tested for statistical overrepresentation of Gene Ontology (GO) BP terms using Pantherdb.org [47]. Insulin-positive mouse cells were analysed in a similar manner except that putative hub cells were classified as the intersection between the upper quartile of *Gck* expression and the lower two quartiles of *Ins1* expression.

Statistical analysis.

Statistical significance between two conditions was assessed using paired or unpaired Student's t-test. Interactions between multiple conditions were determined using one- or two-way ANOVA (with Tukey's or Bonferroni posthoc tests). Analyses were performed using Graph Pad Prism (GraphPad Software version 8.0) and MATLAB (Mathworks) and significant p-values are described in each relevant section. Values are plotted as mean ± SEM, unless otherwise stated.

Data availability

The data that support the findings of this study and the Matlab codes for the various connectivity analyses described above are available from the corresponding authors upon request. Data repositories for the transcriptomic analyses are referenced in the appropriate sections. The Reporting Summary for this manuscript, which details experimental design, statistical analyses and reagents is available as a separate document. No datasets were excluded from the mouse experiments and in all cases (except for the human diabetic islet experiments, as described) the connectivity results between low and high glucose states were in the same direction.

RESULTS

Glucose controls β cell connectivity in the living zebrafish.

To explore Ca^{2+} dynamics *in vivo* with single-cell resolution we first imaged at low acquisition speeds (0.1 Hz; Supplementary Figure 1a) zebrafish larvae (4-5dpf) expressing GCaMP6s under the insulin promoter (Figure 1a) and the nuclear β-cell marker *Tg(ins:cdt1-mCherry)*, which marks 86 ± 6.6 % (*n*=5 islets) of all β-cells at 5 dpf. We focused our study on the primary zebrafish islet, which is the only islet present at this stage. We first used *ex vivo* imaging to directly compare the glucose-responsiveness of the primary and secondary islets dissected from adult fish[35]. As expected, β cells from the primary and secondary islets showed apparent Ca^{2+} influx upon stimulation with 10 and 20 mM glucose or depolarization with potassium chloride (KCl; *n*=3 primary and *n*=3 secondary islets) (Supplementary Movie 1). Thus, the primary islet is an adequate system for studying the glucose-stimulated Ca^{2+} dynamics in zebrafish β cells, as well as representing the major site of insulin storage.

In vivo imaging of GCaMP6s-expressing β cells in larvae revealed the existence of endogenous oscillations in cytosolic free Ca^{2+} (12/12 animals studied; Supplementary Figure 1 a-c, Supplementary Movie 2). This activity was inhibited by intracardiac injection of insulin, which lowered whole-animal glucose (Supplementary Figure 1, c-f, Supplementary Movie 3), indicating that the oscillatory Ca^{2+} signal was due to elevated circulating levels of glucose that are measurable by 4-5 dpf [48]. Ca^{2+} dynamics were also decreased after a transient suppression of blood flow by a temporally controlled heart block (Supplementary Movie 4). Time-lapse imaging of red-blood cells and β cells confirmed that the zebrafish islet is perfused in larvae (Supplementary Movie 5). Taken together, these results reveal endogenous β cell Ca^{2+} oscillations likely to be involved in the systemic sensing of glucose *in vivo* in the zebrafish.

We next explored the impact of increasing the levels of glucose in the zebrafish circulation. We performed intra-cardiac injection of glucose, allowing for rapid entry of the sugar into the circulation (Figure 1b-d). After a short lag (20-50 s) this manoeuvre led to a rapid increase in cytosolic Ca^{2+} concentrations (assessed as the time take to achieve a GCaMP6 signal >20% above baseline) in β cells across the islet (Figure 2 b-d; Supplementary Movie 6), and corresponded to the time-dependent increases in whole animal glucose concentrations assessed separately (Figure 1e).

We next sought to determine the degree to which the β cell population in these experiments was connected before and after stimulation with glucose, firstly at low imaging speeds of

0.1Hz (Figure 2 and Supplementary Figure 2) then at high imaging speeds of 3 Hz (Figure 3a-d). We derived Pearson-based functional connectivity maps (see Methods) of pairwise comparisons between the Ca^{2+} traces of individual cells [21, 49]. At low imaging speeds, 10-15% of cells hosted a connection to another cell prior to glucose injection, and this rose significantly to ~50 % after glucose injection ($p<0.001$, Figure 2 c-f). A similar, dramatic increase ($p<0.01$) was seen for connection strength (i.e. Pearson's correlation, R; Figure 2e). Of note, the temporally-defined "leader" cells (first responders to glucose stimulation) were amongst the most highly connected. For example, in the animal shown in Figure 2, Ca^{2+} increases were first observed in two out of nine cells (cell 2 and cell 6; Figure 2b), and these cells were the most connected on Pearson analysis at high glucose (connected to seven or eight other cells out of a total of nine analysed; Supplementary Table 1).

Recorded at a higher acquisition rate (3 Hz) across a single plane, β cells again displayed modest connectivity at low glucose (pre-injection ~20%; Figure 3d). The increases in intracellular Ca^{2+} which followed glucose injection (Figure 3a and b) were associated with a significant rise in correlation coefficient (Figure 3c) as well as a marked increase in the number of functionally-connected cell pairs (post-injection ~88%, $p<0.0001$, Figure 3d). Approached with a Pearson analysis at high glucose, essentially every cell became strongly connected to every other cell. Finally, whole islet live-imaging at an acquisition rate of 0.8Hz, covering ~700μm^3 was achieved. In this way, it was possible to resolve the majority (20) cells within the primary islet of the zebrafish (Figure 3e) and extract their signal spatially in three dimensions (Figure 3f; Supplementary Movie 7). We then undertook 3D connectivity analysis on three separate zebrafish islets before and after glucose stimulation (as before). Figure 3g shows the 3-dimensional connectivity analysis for one fish islet with mean coefficient of correlation rising from 40.1 to 89.1 and fraction of connected cells rising from 11.2 to 92.3 % with a glucose bolus. Results for the other two islets showed the same rise in Pearson coefficient (83.2 to 91.7 and 44.9 to 85.1) and rise in connected cells (33.3 to 55.5% and 16.7 to 38.1%). We therefore conclude that functional connectivity occurs across the entire fish islet and that 2-dimensional (single plane) connectivity analysis in the fish accurately reflects what occurs across the entire islet.

Ablation of leader cells prevents subsequent Ca^{2+} waves in the zebrafish embryo.

In order to determine whether "leader" (first responder) cells may serve a regulatory role, as demonstrated previously for mouse islets *in vitro* [21], we used cell ablation through two photon laser irradiation (Figure 4, Supplementary Movies 8 and 9). Animals were challenged with three separate pulses of intracardiac glucose introduced before and after irradiation of

either leader or follower cells (*n*=20 leader and *n*=20 follower cell ablation experiments). Whereas ablation of follower cells had no discernible effect on the subsequent Ca^{2+} spikes, ablation of leader cells led to a significant reduction in the total islet GCaMP response (Figure 4). Only targeted cells revealed evidence of nuclear destruction, while the neighbouring cells showed no obvious damage (Supplementary Figure 4). Moreover, we show that islet blood flow remains unaltered following the ablation of the cells using bright-field imaging before and after the ablation (Supplementary Movies 8 and 9). Thus, the targeted ablation of a single β cell in vivo does not appear to perturb either local endothelial cells or the rest of the β cells in the islet.

Leader cells do not preferentially derive from the dorsal or ventral buds in the zebrafish embryo.

The primary zebrafish islet contains both dorsal bud-derived β cells (DBCs) and ventral bud-derived β cells (VBCs). To interrogate whether embryonic derivation affected the identity of leader cells, we performed injection of mRNA encoding H2B-RFP to distinguish between D- and VBCs based on label dilution [34]. In this assay, DBCs retain the H2B-RFP label whereas VBCs dilute it. We performed 4D live Ca^{2+} imaging and glucose injections in these embryos. In the three islets examined, two revealed label-retaining cells as leaders, meanwhile one islet revealed a leader cell that was H2B-negative. Supplementary Movie 10 shows a 3D reconstruction of one representative experiment in which the leader cell was H2B-RFP-positive. This implies that both the D- and VBCs can become leader cells. It is important to note that, in these experiments, we did not observe impaired responsiveness of DBCs to glucose stimulation *per se*, indicating that DBCs indeed exhibit characteristics of functional β cells.

Glucose enhances Ca^{2+} dynamics and elicits increases in β cell-β cell connectivity in islets in the living mouse.

We next extended our analysis to islets from the adult mouse, with superficial β cell layers infected with adenoviral GCaMP6m, before engraftment into the anterior chamber of a recipient mouse eye (ACE) [22]. Non-β cells are not infected by this protocol due to the absence of the cognate receptor (Coxsackie virus receptor [50]). Using animals maintained under general anaesthetic, we collected data at acquisition speeds of 1 Hz, before and after IP glucose injection (see Methods).

663 Ca^{2+} dynamics were increased in response to a rise in circulating glucose.The proportion of
664 significantly Pearson-connected cells increased on average from 38 ± 11% to 65 ± 9% (*n*=5
665 islets in 5 animals, p=0.028) with a non-significant (*p*=0.11) rise in the mean coefficient of
666 connectivity from 0.54 ± 0.03% to 0.63 ± 0.04%.
667
668 We subsequently generated islets from transgenic mice expressing GCaMP6f highly
669 selectively in the β cell, under the control of *Cre* recombinase expressed from the *Ins1* locus
670 [39, 40], and transplanted into the mouse ACE as above. Almost every β cell (~95%) [21] within
671 the transgenic islet expressed the Ca^{2+} probe, allowing us to interrogate the activity of many
672 more cells per islet, including those localised more deeply in the islet core (typically 50 to
673 100). We captured data at higher rates (up to 3 Hz) under low and high circulating glucose
674 conditions (see Methods).
675
676 Strikingly, and in contrast to islets infected with adenoviral GCaMP6f, we observed wave-like
677 behaviour of the β cell Ca^{2+} increases in all islets (examined separately and in ten different
678 animals) at high circulating glucose levels (Supplementary Movies 11, 12 and 13, Figure 5b
679 and 6c). Ca^{2+} waves were initiated at discrete sites (Supplementary Movie 12), with
680 propagation velocities of 12.0 ± 3.4 μm/s (*n*=5 wave bursts). As shown in the example in
681 Figure 5B and Supplementary Movie 13, whilst most cells were quiescent under low glucose
682 conditions, high circulating glucose levels was associated with runs of highly-coordinated
683 oscillations, even after prolonged glucose exposure (10 minutes, Figure 5b and Figure 6a).
684
685 We were able to quantify connectivity using both Pearson and binarized data approaches
686 (Figures 5 and 6). As observed in the fish, high circulating glucose was associated with a
687 significantly higher mean coefficient of connectivity, and proportion of connected cells,
688 versus the low glucose condition, as revealed by Pearson analysis (Figures 5 c-e and
689 Supplementary Figure 5a). We also used a piezo device to allow for fast acquisition of β cell
690 readouts in three separate cell layers under low and high circulating glucose conditions, to
691 investigate whether β cell connectivity existed in 3-dimensions (see Methods). Of note, this
692 significant rise in pan-islet β cell connectivity at high circulating glucose levels also occurred
693 between cells that were more than a layer apart on 3D imaging (Figure 5c-e and
694 Supplementary Figure 5a). The Pearson analysis was, however, unable to detect significant
695 differences in co-activities required for identification of super-connected cells/hubs. In
696 contrast, application of a binarized approach (see Methods) [21] revealed scale free network
697 topography in which 8.7 ± 3.7% of cells hosted the majority (60-100%) of connections
698 (Figures 6 a-b and Supplementary Figure 6). Pooled over all five islets examined, the R^2
699 value for this power law distribution was 0.62.

Finally, we examined islet Ca^{2+} dynamics over 10 minutes at steady state high glucose levels (and also acquired medium and low glucose acquisitions from the same cells in the same 1 h-long imaging study), to exclude the possibility that pan-islet connectivity is related to spatially aggregated β cells simply responding acutely and synchronously to a rise in circulating glucose concentration. Blood sugar readings recorded over these imaging sessions did not reveal oscillating glucose levels, excluding the trivial possibility that glucose oscillations themselves are driving Ca^{2+} oscillations (Figure 5b). A concerted, elevated Pearson correlation and percentage β cell connectivity was achieved over these longer acquisitions with higher (and sustained) circulating glucose levels (Figure 6a).

Prospective analysis (Granger causality)

Given the challenges of a direct interventional strategy such as photo-ablation in the mouse eye, we deployed an alternative, mathematical approach to examine the potential role of leader cells as pacemakers. Granger analysis [32] provides a means of assessing whether a given time series may be useful in forecasting another, i.e. is predictive of a causal relationship. This supported our visual identification of first responding (leader) cells. As shown in Figure 6 c-e, we observed that those four cells ("leaders", Figure 6C; this islet is shown in Supplementary Movie 11), which fired first during a prolonged run of Ca^{2+} pulses, were always represented as leaders in the second and third bursts but not always in fourth and fifth bursts (if present). However, leader cells identified temporally as among the first five responding cells under high glucose conditions were invariably the most highly connected on independent Granger analysis (Supplementary Table 2). Granger analysis of the top 10 most highly connected cells during the prolonged imaging sessions (10 minute acquisitions at high, medium and low glucose, of the same cross section of islet/same β cell ROIs) revealed one cell to be a Granger leader in all three states and, interestingly, to be in the same region (neighbouring) 2-5 other Granger leaders in the medium and high state – which was also the segment of islet from which waves emanated (data not shown).

Interestingly, this analysis provided no evidence that peri-capillary cells were more likely to be "Granger leaders" (average distance from leader cells to the nearest capillary: 2.2 ± 1.9 μm *versus* 2.3 ± 1.8 μm for follower cells, n=25, $p>0.05$). Hence, differences between cells in the arrival time for glucose from the blood stream are unlikely to be the determining factor for initiating Ca^{2+} waves.

Engrafted human islets are highly connected.

To corroborate our findings in a further species we studied the behaviour of 11 human islets transduced with AV-GCaMP6m and transplanted into the ACE of (immunocompromised) BALB/c *nu/nu* mice (see Methods) We observed a non-significant rise in human islet coefficient of correlation from 0.39 to 0.59, and a corresponding rise in β cell connectivity from 56% to 76% between low and high circulating glucose conditions (Supplementary Figure 5b). Intriguingly, in the two islets that came from a donor with longstanding Type 2 Diabetes (see Methods), the switch from low to high circulating blood sugar was associated with an unexpected drop in Pearson R (53 to 24 and 44 to 32), and an equivalent fall in the proportion of connected β cells (from 30% to 20% and 29% to 27%; Supplementary Figure 5c). This observation opens up the possibility that the loss of insulin secretory function that occurs in Type 2 diabetes is linked to abnormal connectivity patterns.

Transcriptomic analysis.

To determine whether hub/leader cells may possess a discrete molecular signature *versus* followers we analysed RNASeq data from fish and mouse β cells. We have previously reported [21] that hub cells in the mouse islet are characterised by relatively high levels of glucokinase (Gck) immunoreactivity, and lower levels of Insulin, Pdx1, Nkx6,1 staining.

We first generated and analysed a zebrafish transcriptomic data set (10x Genomics) and were able to identify a cluster of mainly endocrine cells expressing *sst1.1*, *gcga* or *ins*. Further clustering of these 'endocrine' cells produced clusters of likely delta (*sst1.1*), alpha (*gcga*) and β (*ins*) cells (Supplementary Figure 6a-b). Putative hub cells were identified based on the higher glucokinase and lower insulin expression previously observed in mouse islets. The intersection of the upper quartile of *gck* expression and the lower quartile of *ins* expression identified 9 % of β cells as putative hub cells (Supplementary Figure 6c). Enrichment and gene ontology (GO) analysis revealed elevated expression of genes in hub/leaders associated with mitochondrial metabolism (oxidative phosphorylation and respiratory electron transport chain) and generation of precursor metabolites and energy, among other terms (Supplementary Figure 6 d-e). Interestingly, the re-clustering of the 'endocrine' cluster resulted in two distinct and approximately equally-sized β cell populations. The putative hub cells identified here came almost entirely from a single cluster, suggesting these may represent one end of a continuous distribution within this cluster rather than a distinct subset.

Similar analysis of mouse islet data revealed that the intersection of the upper quartile of *Gck* and lower two quartiles of *Ins1* expression contained 11 % of β cells (Supplementary Figure 6 f-h). Genes upregulated in this cluster were overrepresented in the GO terms "Glycolysis" and "Generation of precursor metabolites and energy" (Supplementary Figure 6 i-j), potentially indicating that these are more metabolically active cells, as observed above in the zebrafish case.

DISCUSSION

The principal aim of the present study was to explore β cell coordination in the islet *in vivo* in the living animal. Here, we have studied the zebrafish islet in its natural state and the mouse islet under conditions of vascularisation and innervation which closely recapitulate those of the islet within the pancreas [51-53]. We show that, despite the quite profound differences between the isolated and *in vivo* islet, coordinated β cell responses to glucose stimulation display many of the features previously described *in vitro*, including the emergence of cells which may govern islet-wide Ca^{2+} dynamics and hence pulsatile insulin secretion.

Islet-wide Ca^{2+} dynamics in the living zebrafish

We demonstrate firstly that, in the zebrafish, increases in blood glucose lead to a coordinated increase in β cell cytosolic Ca^{2+} across the islet. Using Pearson R analysis, we describe a well-connected network of β cells in the zebrafish islet that responded in a coordinated fashion to glucose stimulation. These findings align well with those of Markovic *et al* [49] in murine pancreatic slices, and our own findings in isolated mouse islets [18]. Given the small size of the zebrafish islet at this developmental stage, it was not possible to apply scale-free network theory to these datasets. However, we were able, using a direct interventional approach akin to the use of optogenetics in isolated murine islets[21, 54], to demonstrate that those cells which were the first to exhibit a Ca^{2+} increase ("leaders") may perform a role as regulators of the activity of other β cells. Photo-ablation of leader, but not follower cells, resulted in a significant abrogation of Ca^{2+} dynamics in remaining β cells in terms of their time to response as well as their overall calcium response to a glucose challenge. We also provided evidence to establish that this methodology produced no collateral damage, i.e. did not affect cells other than the single β cell that was targeted. We would emphasize that this approach offers significant advantages over the use of optogenetics for β cell targeting, notably the fact that further genetic modification required to express an optogene (e.g. a photoswitchable channel or pump- shown to influence β cell activity) [21, 54, 55] is avoided, and axial resolution is high. Photo-ablation of leader, but not follower cells, resulted in the abrogation of Ca^{2+} dynamics (Fig. 4c), pointing to a role for the former as regulators of β cell activity across the islet.

It was particularly interesting to note the findings of the *ex vivo* imaging studies that directly compared *in vitro* glucose-responsiveness of the primary and secondary zebrafish islets. The only discernible difference we observed between the primary and the much later-forming secondary islets *ex vivo* pertained to a faster Ca^{2+} response of the latter, which was

evident at 10 mM glucose. This faster response is likely to reflect the much smaller size of the secondary islets and, hence, the easier penetration to the islet core of glucose when added *ex vivo*. It is important to note also that we have not observed impaired responsiveness to glucose stimulation of β cells originating from the dorsal pancreatic buds *in vivo*, consistent with our recent findings that DBCs are functional [26]. Finally, when imaged in culture, the zebrafish islets exhibit seemingly uncoupled behaviours, revealing the glucose-sensitivity of individual β-cells [26,56]. In contrast, β-cells show synchronized responses to glucose *in vivo* (this study and [56]). Thus, the unperturbed conditions of the *in vivo* environment might be critical for the coupling of β-cells.

Islet-wide Ca^{2+} dynamics in the engrafted mouse islet

In mammalian islets, we routinely observed clear trans-islet, glucose-induced Ca^{2+} waves (10/10 Ins1Cre-GCaMP6-expressing islets examined in independent experiments), whereas these are not always observed in Fluo8-loaded isolated islets *in vitro* [21]. This may reflect the presence of nerves and blood vessels in our *in vivo* model as well as, conceivably, the better preservation of β cell identity, gap junctions, etc. [2]. Moreover, the use of transgenic islets, in which the genetically-encoded Ca^{2+} sensor is present in almost the entire (~95%) β cell population after recombination using the Ins1Cre transgene [21, 39, 40], is likely to facilitate the detection of waves. Thus, we were able to image cells located some distance away from the islet periphery, with adequate resolution to 4-5 cell depths in the z-plane (Supplementary Movie 14). Furthermore, with a rapid piezo device we were able to demonstrate that Ca^{2+} dynamics were strongly coordinated across β cells that were separated by another layer of cells. However, the present studies do not address the question of how connections across the islet are established (e.g. roles for islet inter-neurons, paracrine factors, etc.). Other interventional approaches (e.g. using multiphoton, light sheet or other imaging techniques) will be necessary to explore these phenomena in the future.

By imaging large numbers of cells simultaneously, and subjecting the resulting datasets to binarization analysis, we revealed the existence of scale free networks, as previously described *in vitro* [21]. This set of experiments examined the nature of islet behaviour *in vivo* through two different but complementary lenses. Pearson R analysis highlights the pan-islet β cell connectivity (both in terms of the number of connected cells and their strength of correlation) in response to elevated circulating glucose levels. Separately, we have demonstrated using data binarization and shuffling [21] that these cells are connected in a way

that fits with the presence of super-connected hubs. Recently, Rupnik and colleagues [57] have reported, using mouse islets located within pancreatic slices, that at adequate acquisition speeds (10Hz), Pearson analysis can reveal a connectivity probability distribution function that obeys a power law, at least initially following glucose stimulation.

To corroborate our zebrafish findings, where disruption of the temporally-defined "leader" cells abrogated subsequent islet-wide Ca^{2+} responses to glucose, we performed independent mathematical causality analysis of all the β cells that were recorded in the mouse islet. Selecting a causality time lag consistent with that observed between the first responders and the rest of the β cells (i.e. 1 s) [32], we revealed that these were indeed the most highly causally linked to the activity of all other cells in the islet. Both the experimentally established zebrafish "leaders" and the mathematically causally-identified mouse "leaders" are reminiscent of previously identified *in vitro* hub cells [21], insofar as both regulate Ca^{2+} dynamics observed in the rest of the islet being imaged. Our present findings also indicate that temporal and spatial dynamics need to be considered in identifying likely regulatory populations. For example, essentially normal blood flow is maintained in the engrafted islet. One may have predicted, therefore, that "leader" β cells would be those located immediately adjacent to blood vessels. In contrast, we observed no greater likelihood of cells in this domain of the islet initiating waves than for cells more remotely located. We also observed that islets retained a baseline Ca^{2+} activity (and indeed a degree of connectedness between β cells) even in the low glucose state. Thus, at low circulating glucose levels Ca^{2+} waves were occasionally observed above noise levels with the same amplitude and frequency of bursts as at high glucose, but less commonly. Within a single train of waves, the starting point was often, but not always conserved, and was frequently seen at the islet rim. Such waves often propagated circumferentially, although there were some that appeared to move towards the islet core. Taken together, this hints that functional networks already exist at low glucose concentrations, under conditions in which the majority of cells are not yet firing. These pre-activated networks may then expand and work as a coordinating unit to drive the recruitment of followers.

It was also important to demonstrate a retention of the high connectivity readouts in islets that had been exposed to prolonged elevated glucose levels. Many previous studies on isolated islets and β cells reveal heterogeneous Ca^{2+} responses to glucose stimulation [58]. Indeed, we are not aware of existing literature supporting the notion that β cells have an identifiable (and identical) resting Ca^{2+} oscillation signature. Nevertheless, it was important here to exclude the possibility that the high connectivity observed at high glucose levels is a

phenomenon related to spatially aggregated (i.e. intra-islet) β cells simply responding acutely and synchronously to a rise in circulating glucose concentration. The high connectivity findings in islets that had been imaged for an hour at elevated circulating glucose levels serve to argue against the possibility that connectivity is an acute phenomenon of this type since, in an uncoordinated system, over a 60 min. imaging protocol, with glucose levels that are not rapidly varying, one would expect de-synchrony to emerge. Finally, the first responders (and Granger leaders) are defined during Ca^{2+} pulses at essentially constant glucose (although glucose may drift gradually over multiple Ca^{2+} waves during these recordings).

Several questions remain with respect to the Ca^{2+} waves identified here: to what extent are their starting points spatially defined relative to nerves and other islet cell types? How do they propagate? Are they always associated with pulses of insulin secretion? Further studies are also required to determine whether "leader" cells are functionally essential to islet health, are pre-fated or can assume leader characteristics over time that relate to altered islet function under metabolic stress or in diabetes.

Towards the molecular identity of hub/leader cells

Prior to the current study, our understanding of the differences in molecular identity between hub and follower cells was fragmentary [21]. To explore this question here in an unbiased, transcriptome-wide manner, we have leveraged the known properties of mouse hub cells, i.e. elevated expression (at the protein level) of *Gck* and relatively weak expression of *Insulin*. We note that confirmation of similar properties for the fish hub/follower populations (i.e. high *Gck*/low *insulin*/low *Pdx1*-immunoreactivity) was not possible here due to the absence of suitable antibodies for the *D. rerio* Gck protein. Nonetheless, if we assume similar properties for the fish and mouse hub cells our analyses reveal that, in both species, a population exists with characteristics which may be expected of these cells, notably elevated expression of genes involved in glucose metabolism and, in zebrafish, of genes involved in mitochondrial metabolism. Of note, a similar β cell population was identified recently in the mouse by Pospisilik and colleagues [59]. Future studies, involving the direct isolation of hubs and followers based on function (e.g. Ca^{2+} dynamics), are needed to confirm or refute these findings.

Summary

In conclusion, we show here that examined in the living animal β cells within the islet are highly connected in three dimensions and that this connectivity is tightened in response to a glucose challenge. As predicted from previous studies of isolated islets *in vitro* [18, 21], we show that critical subpopulations of β cells, which appear to generate Ca^{2+} waves, serve a regulatory role in the zebrafish and appear likely to do so in the mammalian islet as well. At this stage, it is not possible to investigate whether the leader cells are a distinct population with a distinct origin and development. However, we provide a preliminary analysis, using an imputation approach based on previously-described proteomic properties of these populations [21], to suggest they possess a distinct transcriptomic signature. Future challenges will involve isolating and characterising these cells, as well as assessing the stability of each sub group (i.e. leader/hubs and followers). Taken together, our data provide further evidence for a division of labour within the islet *in vivo* in three different species, reinforcing the importance of β cell heterogeneity for normal glucose-responsiveness.

Acknowledgements.

VS was supported by a Diabetes UK Harry Keen Clinician Scientist 15/0005317. G.A.R. was supported by a Wellcome Trust Senior Investigator Award (WT098424AIA), MRC Programme grants (MR/R022259/1, MR/J0003042/1, MR/L020149/1) and Experimental Challenge Grant (DIVA, MR/L02036X/1), MRC (MR/N00275X/1), Diabetes UK (BDA/11/0004210, BDA/15/0005275, BDA 16/0005485) and Imperial Confidence in Concept (ICiC) grants, and a Royal Society Wolfson Research Merit Award. I.L. was supported by Diabetes UK Project Grant 16/0005485 and D.J.H. by a Diabetes UK R.D. Lawrence (12/0004431) Fellowship, a Wellcome Trust Institutional Support Award, and MRC (MR/N00275X/1) and Diabetes UK (17/0005681) Project Grants. N.N. received funding from the DFG–Center for Regenerative Therapies Dresden, Cluster of Excellence at TU Dresden and the German Center for Diabetes Research (DZD), as well as research grants from the German Research Foundation (DFG), the European Foundation for the Study of Diabetes (EFSD) and the DZD. L.J.B.B. was supported by a Sir Henry Wellcome Postdoctoral Fellowship (Wellcome Trust, 201325/Z/16/Z) and a Junior Research Fellowship from Trinity College, Oxford. This project has received funding from the European Research Council (ERC) under the European Union's Horizon 2020 research and innovation programme (Starting Grant 715884 to D.J.H.) and from the Innovative Medicines Initiative 2 Joint Undertaking under grant agreement No 115881 (RHAPSODY) to G.A.R. and P.M. This Joint Undertaking receives support from the European Union's Horizon 2020 research and innovation programme and EFPIA. We would like to thank Professor Per-Olof Berggren (Karolinska Institute, Sweden and Imperial College London), Alejandro Caicedo and Raynor

965 Rodriguez (University of Miami), and Drs Pauline Chabosseau, Marie-Sophie Nguyen-Tu
966 and Bryn Owen (Imperial College London), for valuable advice and support with surgery and
967 imaging. With thank Rebecca Callingham (Imperial College) for assistance with human islet
968 culture.

969

970

Author Contributions

VS, NN and GAR designed the study, LDS and NA performed the zebrafish experiments, VS, KS, AMA, and IL undertook the mouse studies, GC and KS performed virus preparations, DCAG, SMR, KS and VS developed movement correction macros, EG, SNMG, NA, TS, DJH and LB contributed to connectivity analysis, DJH and LB provided code for connectivity analysis, VS and WD developed connectivity and Granger scripts and undertook all connectivity analyses, PM and AMJS provided human islets and KS and VS undertook studies on these preparations. TJP, NA and SPS performed transcriptomic and bioinformatics analyses. GAR, VS, LDS and NN wrote the manuscript with contributions from all authors.

G.A.R. has received grant funding from Servier and is a consultant for Sun Pharma. All others authors declare no competing financial interests

985

986

Reference List

1. DeFronzo,R.A., Ferrannini,E., Zimmet,P., & Alberti,G. International Textbook of Diabetes Mellitus 4 th Edition. 2015. Hoboken, New Jersey, Wiley-Blackwell.

2. Rutter,G.A., Pullen,T.J., Hodson,D.J., & Martinez-Sanchez,A. Pancreatic beta cell identity, glucose sensing and the control of insulin secretion. *Biochem. J.* **466**, 202-218 (2015).

3. Tarasov,A.I. *et al.* The mitochondrial Ca^{2+} uniporter MCU is essential for glucose-induced ATP increases in pancreatic â-cells. *PLoS One* **7**, e39722 (2012).

4. Xin,Y. *et al.* RNA Sequencing of Single Human Islet Cells Reveals Type 2 Diabetes Genes. *Cell Metab.* **24**, 608-615 (2016).

5. Segerstolpe,A. *et al.* Single-Cell Transcriptome Profiling of Human Pancreatic Islets in Health and Type 2 Diabetes. *Cell Metab.* **24**, 593-607 (2016).

6. Li,J. *et al.* Single-cell transcriptomes reveal characteristic features of human pancreatic islet cell types. *EMBO Rep.* **17**, 178-187 (2016).

7. Wang,Y.J. *et al.* Single-Cell Transcriptomics of the Human Endocrine Pancreas. *Diabetes.* **65**, 3028-3038 (2016).

8. Kiekens,R. *et al.* Differences in glucose recognition by individual rat pancreatic B cells are associated with intercellular differences in glucose-induced biosynthetic activity. *J. Clin. Invest.* **89**, 117-125 (1992).

9. Ammala,C. *et al.* Inositol trisphosphate-dependent periodic activation of a Ca2+-activated K+ conductance in glucose-stimulated pancreatic β-cells. *Nature* **353**, 849-852 (1991).

10. Benninger,R.K. & Piston,D.W. Cellular communication and heterogeneity in pancreatic islet insulin secretion dynamics. *Trends Endocrinol. Metab.* **25**, 399-406 (2014).

11. Meda,P. *et al.* The topography of electrical synchrony among beta-cells in the mouse islet of Langerhans. *Q. J. Exp. Physiol.* **69**, 719-735 (1984).

12. Palti,Y., David,G.B., Lachov,E., Mida,Y.H., & Schatzberger,R. Islets of Langerhans generate wavelike electric activity modulated by glucose concentration. *Diabetes.* **45**, 595-601 (1996).

13. Benninger,R.K., Zhang,M., Head,W.S., Satin,L.S., & Piston,D.W. Gap junction coupling and calcium waves in the pancreatic islet. *Biophys. J.* **95**, 5048-5061 (2008).

14. Head,W.S. *et al.* Connexin-36 gap junctions regulate in vivo first- and second-phase insulin secretion dynamics and glucose tolerance in the conscious mouse. *Diabetes.* **61**, 1700-1707 (2012).

15. Meda,P., Kohen,E., Kohen,C., Rabinovitch,A., & Orci,L. Direct communication of homologous and heterologous endocrine islet cells in culture. *J. Cell Biol.* **92**, 221-226 (1982).

16. Meda,P., Santos,R.M., & Atwater,I. Direct identification of electrophysiologically monitored cells within intact mouse islets of Langerhans. *Diabetes* **35**, 232-236 (1986).

17. Rutter,G.A. & Hodson,D.J. Beta cell connectivity in pancreatic islets: a type 2 diabetes target? *Cell Mol. Life Sci.* **72**, 453-467 (2015).

18. Hodson,D.J. *et al.* Lipotoxicity disrupts incretin-regulated human beta cell connectivity. *J. Clin. Invest.* **123**, 4182-4194 (2013).

19. Stozer,A. *et al.* Functional connectivity in islets of Langerhans from mouse pancreas tissue slices. *PLoS Comput. Biol.* **9**, e1002923 (2013).

20. Hodson,D.J. *et al.* Existence of long-lasting experience-dependent plasticity in endocrine cell networks. *Nat. Commun.* **3**, 605 (2012).

21. Johnston,N.R. *et al.* Beta cell hubs dictate pancreatic islet responses to glucose. *Cell Metabolism* **24**, 389-401 (2016).

22. Speier,S. *et al.* Noninvasive in vivo imaging of pancreatic islet cell biology. *Nat. Med.* **14**, 574-578 (2008).

23. Tian,L. *et al.* Imaging neural activity in worms, flies and mice with improved GCaMP calcium indicators. *Nat. Methods.* **6**, 875-881 (2009).

24. van der Meulen,T. *et al.* Virgin Beta Cells Persist throughout Life at a Neogenic Niche within Pancreatic Islets. *Cell Metab.* **25**, 911-926 (2017).

25. Chen,C. *et al.* Alterations in beta-Cell Calcium Dynamics and Efficacy Outweigh Islet Mass Adaptation in Compensation of Insulin Resistance and Prediabetes Onset. *Diabetes.* **65**, 2676-2685 (2016).

26. Singh,S.P. *et al.* Different developmental histories of beta-cells generate functional and proliferative heterogeneity during islet growth. *Nat. Commun.* **8**, 664-00461 (2017).

27. Kimmel,R.A. & Meyer,D. Zebrafish pancreas as a model for development and disease. *Methods Cell Biol.* **134**, 431-461 (2016).

28. Steiner,D.J., Kim,A., Miller,K., & Hara,M. Pancreatic islet plasticity: interspecies comparison of islet architecture and composition. *Islets.* **2**, 135-145 (2010).

29. Bosco,D. *et al.* Unique arrangement of alpha- and beta-cells in human islets of Langerhans. *Diabetes.* **59**, 1202-1210 (2010).

30. Prince,V.E., Anderson,R.M., & Dalgin,G. Zebrafish Pancreas Development and Regeneration: Fishing for Diabetes Therapies. *Curr. Top. Dev. Biol.* **124:** 235-276 (2017).

31. Ninov,N. *et al.* Metabolic regulation of cellular plasticity in the pancreas. *Curr. Biol.* **23**, 1242-1250 (2013).

32. Granger,C.W.J. Investigating Causal Relations by Econometric Models and Cross-spectral Methods. *Econometrica* **37**, 424-438 (1969).

33. Barnett,L. & Seth,A.K. The MVGC multivariate Granger causality toolbox: a new approach to Granger-causal inference. *J. Neurosci. Methods.* **223**, 50-68 (2014).

34. Hesselson,D., Anderson,R.M., Beinat,M., & Stainier,D.Y. Distinct populations of quiescent and proliferative pancreatic beta-cells identified by HOTcre mediated labeling. *Proc. Natl. Acad. Sci. U. S. A.* **106**, 14896-14901 (2009).

35. Janjuha,S., Pal,S.S., & Ninov,N. Analysis of Beta-cell Function Using Single-cell Resolution Calcium Imaging in Zebrafish Islets. *J. Vis. Exp.*10 (2018).

36. Schindelin,J. *et al.* Fiji: an open-source platform for biological-image analysis. *Nat. Methods.* **9**, 676-682 (2012).

37. Ollion,J., Cochennec,J., Loll,F., Escude,C., & Boudier,T. TANGO: a generic tool for high-throughput 3D image analysis for studying nuclear organization. *Bioinformatics.* **29**, 1840-1841 (2013).

38. Preibisch,S., Saalfeld,S., Schindelin,J., & Tomancak,P. Software for bead-based registration of selective plane illumination microscopy data. *Nat. Methods.* **7**, 418-419 (2010).

39. Kone,M. *et al.* LKB1 and AMPK differentially regulate pancreatic beta-cell identity. *FASEB J.* **28**, 4972-4985 (2014).

40. Thorens,B. *et al.* Ins1 knock-in mice for beta cell-specific gene recombination. *Diabetologia* **58**, 558-656 (2015).

41. Luo,J. *et al.* A protocol for rapid generation of recombinant adenoviruses using the AdEasy system. *Nat. Protoc.* **2**, 1236-1247 (2007).

42. Ravier,M.A. & Rutter,G.A. Isolation and culture of mouse pancreatic islets for ex vivo imaging studies with trappable or recombinant fluorescent probes. *Methods Mol. Biol.* **633**, 171-184 (2010).

43. Janjuha,S. *et al.* Age-related islet inflammation marks the proliferative decline of pancreatic beta-cells in zebrafish. *Elife.* **7.**, 32965 (2018).

44. Zheng,G.X. *et al.* Massively parallel digital transcriptional profiling of single cells. *Nat. Commun.* **8:**14049 (2017).

45. Baron,M. *et al.* A Single-Cell Transcriptomic Map of the Human and Mouse Pancreas Reveals Inter- and Intra-cell Population Structure. *Cell Syst.* **3**, 346-360 (2016).

46. Butler,A., Hoffman,P., Smibert,P., Papalexi,E., & Satija,R. Integrating single-cell transcriptomic data across different conditions, technologies, and species. *Nat. Biotechnol.* **36**, 411-420 (2018).

47. Mi,H. *et al.* PANTHER version 11: expanded annotation data from Gene Ontology and Reactome pathways, and data analysis tool enhancements. *Nucleic Acids Res.* **45**, D183-D189 (2017).

48. Gut,P. *et al.* Whole-organism screening for gluconeogenesis identifies activators of fasting metabolism. *Nat. Chem. Biol.* **9**, 97-104 (2013).

49. Markovic,R. *et al.* Progressive glucose stimulation of islet beta cells reveals a transition from segregated to integrated modular functional connectivity patterns. *Sci. Rep.* **5**, 7845 (2015).

50. Diraison,F. *et al.* Over-expression of sterol-regulatory-element-binding protein-1c (SREBP1c) in rat pancreatic islets induces lipogenesis and decreases glucose-stimulated insulin release: modulation by 5-aminoimidazole-4-carboxamide ribonucleoside (AICAR). *Biochem. J.* **378**, 769-778 (2004).

51. Rodriguez-Diaz,R. *et al.* Noninvasive in vivo model demonstrating the effects of autonomic innervation on pancreatic islet function. *Proc. Natl. Acad. Sci. U. S. A.* **109**, 21456-21461 (2012).

52. Ilegems,E. *et al.* Light scattering as an intrinsic indicator for pancreatic islet cell mass and secretion. *Sci. Rep.* **5**, 10740 (2015).

53. Nyqvist,D. *et al.* Donor islet endothelial cells in pancreatic islet revascularization. *Diabetes.* **60**, 2571-2577 (2011).

54. Westacott,M.J., Ludin,N.W.F., & Benninger,R.K.P. Spatially Organized beta-Cell Subpopulations Control Electrical Dynamics across Islets of Langerhans. *Biophys. J.* **113**, 1093-1108 (2017).

55. Reinbothe,T.M., Safi,F., Axelsson,A.S., Mollet,I.G., & Rosengren,A.H. Optogenetic control of insulin secretion in intact pancreatic islets with beta-cell-specific expression of Channelrhodopsin-2. *Islets.* **6**, e28095 (2014).

56. Lorincz,R. *et al.* In vivo monitoring of intracellular Ca(2+) dynamics in the pancreatic beta-cells of zebrafish embryos. *Islets.* **10**, 221-238 (2018).

57. Gosak,M. *et al.* Critical and Supercritical Spatiotemporal Calcium Dynamics in Beta Cells. *Front Physiol.* **8**, 1106 (2017).

58. Ammala,C., Ashcroft,F.M., & Rorsman,P. Calcium-independent potentiation of insulin release by cyclic AMP in single beta-cells. *Nature.* **363**, 356-358 (1993).

59. Lu,T.T. *et al.* The Polycomb-Dependent Epigenome Controls beta Cell Dysfunction, Dedifferentiation, and Diabetes. *Cell Metab.* **27**, 1294-1308 (2018).

Figure legends

Figure 1**. Glucose-stimulated Ca^{2+} influx imaged *in vivo* in the living zebrafish.**
a. Cartoon representing a transgenic zebrafish larva expressing the genetically-encoded Ca^{2+} indicator GCaMP6s (green) and the nuclear marker cdt1-mCherry (red) under the insulin promoter. GCaMP6s allows the examination of glucose-induced Ca^{2+}-influx in the β cell reported by changes in the green fluorescence in a Ca^{2+} concentration-dependent fashion. **b.** Maximum intensity projections of an islet imaged before, during and after the intra-cardiac injection of 5 nL of 25 mM glucose solution. Imaging and glucose stimulation were performed simultaneously. Note the near-synchronous increase in GCaMP6 fluorescence intensity across all the β cells in the islet upon glucose injection. **c.** A trace showing cumulative normalized fluorescent intensity over time for the cells shown in A. The black arrow marks the instance of the glucose injection. **c'.** Normalized fluorescence intensity over time for each individual cell. Each cell is represented by a square. The normalized GCaMP6 fluorescence is displayed as a heat-map, showing the degree of cell activity (*n*=10 animals, not graphically represented here). **d.** Quantification of the islet response to glucose stimulation. The graph depicts the GCaMP6 area under the curve covering 100 seconds before and 100 seconds after the glucose stimulation (*n*=3, paired two tail t-test, P=0.0108, data are means ± SD). The injection of glucose led to a dramatic increase in GCaMP6 fluorescence intensity. **e.** Changes in measured free glucose concentration in larvae following glucose injection as in A. Each dot represents a pool of 10 injected larvae. (*n*=3 for each time point, one-tailed ANOVA, with Tukey's multiple comparisons test, P= 0.0488 for 0 vs. 5min and P= 0.0152 for 5 vs.15min). Data are means ± SD. Scale bars, 10 μm. The cartoons shown in panel (a) belong to the authors of this study. The experiments in **b,c** were performed three independent times with several samples showing similar results. **d** shows a quantification from thee biological replicates from one of the repeats. The experiment in **e** was performed once with multiple samples.

Figure 2. **Ca^{2+} dynamics and connectivity in zebrafish: slow imaging acquisition (frame rate 0.1Hz).**
a. Single confocal planes acquired during each time window (labelled i-v) show an increase in GCaMP fluorescence intensity during time window iii (i.e. coinciding with intracardiac glucose injection) but no strong GCaMP signal before glucose injection (time windows i-ii) or after glucose injection (time windows iv-v). Time windows i-v were 100 s long. **b.** Representation of a normalised fluorescence trace generated by each β-cell region of

interest (ROI) across the entire imaging session (1,200 s). Time windows (100s) labelled i-v are shown at the top and the dashed line represents the time of intra-cardiac glucose injection. T_{20} was defined as the time taken between glucose injection and the calcium intensity spike to reach 20% above baseline. This value is tabulated for each ROI, thereby identifying cell 2 and cell 6 as "leaders". **c.** Cartesian functional connectivity maps displaying the x-y position of analysed cells (numbered black dots). Cells are connected with a coloured line if the p statistic for the Pearson coefficient was < 0.001 post bootstrapping. The strength of the cell pair correlation (the Pearson R statistic) was colour coded: red for R of 0.75 to 1.0, yellow for R of 0.5 to 0.75 and green for R of 0.25-0.5. Results confirm an increase in cell-cell connectivity (strength AND number) during glucose injection (time window iii). **d.** Heat maps show the Pearson coefficient of each cell pair in a colour-coded manner (negative correlation; dark brown (-1), no correlation; mid brown (0), high correlation; yellow/white (1)). **e.** During time window iii (ie at time of glucose injection**)** the mean positive Pearson coefficient for connected cell pairs is 0.75 +/- 4.08 (SEM), significantly higher than before or after glucose injection (window i R 43.8 +/-1.46, ii R 0.48 +/- 2.59, iv R 46.4 +/- 5.3 and v R 0.35 +/- 3.45) ($P<0.001$ on one way ANOVA with Tukey's multiple comparison). **f.** The overall percentage of connected cell pairs is elevated (46% +/- 6.18% SEM) during the glucose injection compared to the rest time points (window i 15.3% +/- 2.4, window ii 10% +/- 1.86, iv 18.6% +/- 4.6 and window v 11.1% +/1 2.7). (n=6, $P<0.001$ one way ANOVA with Tukey's).

Figure 3. **Ca^{2+} dynamics and connectivity examined in zebrafish during rapid image acquisition.**

a. Example islet single confocal slices acquired at 3 frames/s before and during glucose injection. Associated Cartesian connectivity maps and Pearson heatmaps (as described in detail in Figure 2) are given below. **b.** Ca^{2+} traces from individual ROIs in the imaged islet. The dashed line represents the time of intracardiac glucose injection. As described in Figure 2, the time to 20% rise in Ca^{2+} signal post glucose injection was measured, and tabulated in order to identify the first responders or "temporal leaders". **c.** Pooled data for the five animals imaged. The mean Pearson coefficient of correlation rose significantly from the low to high glucose state (n=5, data are means ± SEM, $p<0.001$ on paired two-tailed t-test). **d.** The percentage of significantly connected cell pairs also increases significantly following glucose administration. Data are means±SEM and **p<0.01 following a paired two-tailed t-test). **e.** 3D islet projections acquired at 0.8 Hz before and during glucose injection. **f.** Associated 3D map showing the time of response in a colour-key fashion (red colour

represents the fastest response). **g.** Cartesian connectivity map and Pearson heatmaps for the islet shown in e (*n*=3 animals, not graphically represented here). The experiment in **e,f,g** was performed once with three samples showing similar results.

Figure 4. **Ablation of temporally-defined "leader" cells (but not follower cells) alters islet responsivity to glucose *in vivo* in the zebrafish.**

a-b. Images from the time-lapse recording (six frames/second, single plane) of the islet following three consecutive glucose stimulations before and after "leader" or "follower" (control) cell ablation. Glucose was injected at 5 min. intervals whilst Ca^{2+} dynamics were monitored. After the identification of presumptive "follower" or "leader" cells, these cells were ablated using a two-photon laser ablation (see Methods). An X. indicates the targeted cells. The top panels show representative frames from the movies before and after the ablation of a "follower" (a) or a "leader" cell (b). The lower traces (a'-b') show the normalized GCaMP6 fluorescence traces and the peak in Ca^{2+} influx following glucose injection pre- and post-ablation. **c.** Quantification of the Area Under the Curve (A.U.C.) reflecting 200 frames of normalized GCaMP6 fluorescence before and after the ablation of a "follower" or a "leader" cell (*n* = 20 islets each) (paired two-tailed t-test, P= 3.43 x 10^{-5}, ns: not significant). The ablation of "leader", but not "follower" cells, led to a significant reduction in the total islet GCaMP response. Each data-point represents the mean A.U.C from three glucose-injections in individual larvae. Data are means ± SD. The experiments were performed eight independent times with several samples showing similar results.

Figure 5. **Ca^{2+} waves and connectivity revealed using islets expressing GCaMP6f throughout the cell population under insulin promoter control.**

a. (i) Image of a donor islet that implanted onto the iris of a syngeneic recipient. Islets indicated with arrows. (ii) Individual cells identified within a single islet were analysed. **b.** Imaging for 10 minutes at 1fps of an islet that was exposed to chronically elevated circulating glucose levels (measured values indicated at the time points they were measured along the top). Ca^{2+} traces from 50 individual β cell ROIs are superimposed, demonstrating retained coordination of wave behaviour over time **c.** Pearson heat maps and Cartesian connectivity maps in two dimensions (2D – upper four panels) and 3D (lower four panels). The sharp increase in β cell connectivity occurs in 3D across the entire islet and mirrors what is captured in 2D (single plane). **d** and **e.** Pooled data for the three animals imaged in 3D. Note that the rise in mean Pearson coefficient of β cell connectivity and proportion (%) of cells connected in the low *versus* high glucose state in 3D was comparable to that measured

in 2D. 2D image dataset (*n*=5 islets in 5 different animals, not graphically represented here) revealed a mean rise in Pearson R from 46.4 +/- 7.2 to 92.6 +/- 0.9 ($P<0.01$ on two-tailed t-test) and rise in % connectivity from 19.7 +/- 5.5% to 88.8 +/- 5.9% ($P < 0.001$ on two-tailed t-test).

Figure 6. **Binarized and Granger causality analysis corroborates the existence of super-connected leader cells in mouse islets *in vivo*. a.** Pooled data for average R and % connectivity measurements in mouse islets (n=5 in 5 different animals, individual datapoints shown) imaged over 60 minutes, with prolonged (>10 minute) exposure to high circulating glucose levels. Connectivity was recorded in the high glucose state (>10 mM), medium (6-10mM) and low (<4 mM) state from the same β cell ROIs. Prolonged exposure to high glucose levels does not abrogate the connectivity readout or result in dysynchrony. **b.** Topographic representation of connected β cells as extracted using the binarized and Monte Carlo data analysis approach for the same islet shown in Figure 5. Topographical representation of β cell connections in the remaining four islets imaged are shown in **b'**. The top 20-40% connected cells (reminiscent of previously-defined *in vitro* hubs) are highlighted in white. **c.** Log-log graph of the distribution of cell-cell connections pooled across all five islets imaged reveals a scale-free network (obeying a power-law distribution) whereby 8% cells serve the majority (60-100%) connections. **d**. Section of fluorescence intensity readouts for all 26 cells identified during a typical Ca^{2+} wave (superimposed in different colours) in a single islet. Data collected at 1.0 frame per second, the calcium waves shown here occurred in the high glucose state (25 mM). **e.** Close up of the fluorescent profiles for each individual cell taking part in the islet Ca^{2+} wave. "Leader cells" can be defined temporally as preceding the activity of "follower" cells. **f.** Yellow markers highlight the position of the temporally-defined "leaders". Results are shown in Supplementary Table 1 (Animal #1). Note that temporally the four defined "leaders" are always the most connected on independent Granger Causality analysis.

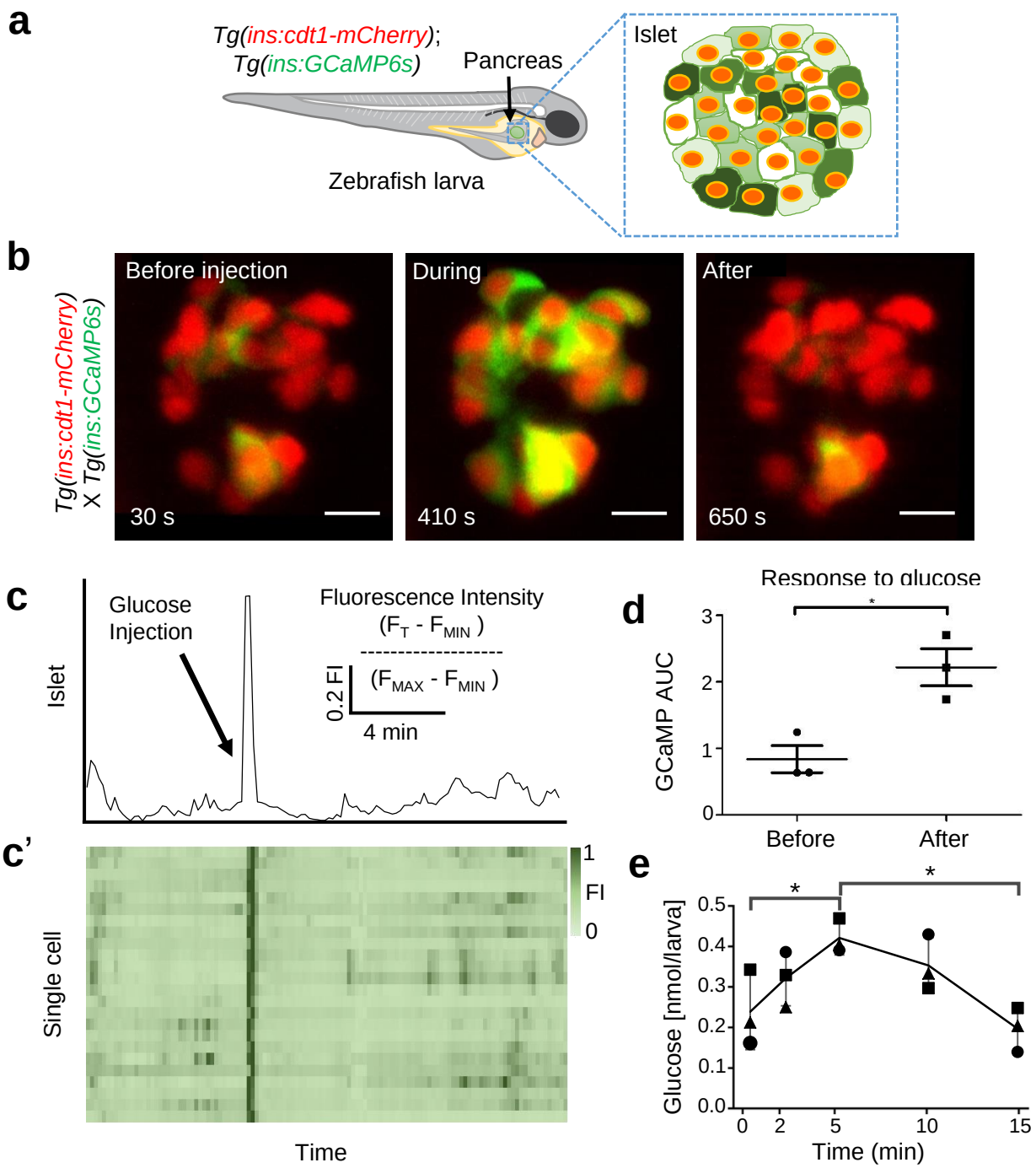
a
Tg(ins:cdt1-mCherry);
Tg(ins:GCaMP6s)
Pancreas
Islet
Zebrafish larva
b
Tg(ins:cdt1-mCherry)
X Tg(ins:GCaMP6s)
Before injection
During
After
30 s
410 s
650 s
c
Glucose
Injection
Islet
Fluorescence Intensity
(F_T - F_MIN)
(F_MAX - F_MIN)
0.2 FI
4 min
c'
Single cell
1
FI
0
Time
d
Response to glucose
GCaMP AUC
Before
After
e
Glucose [nmol/larva]
Time (min)

Figure 1

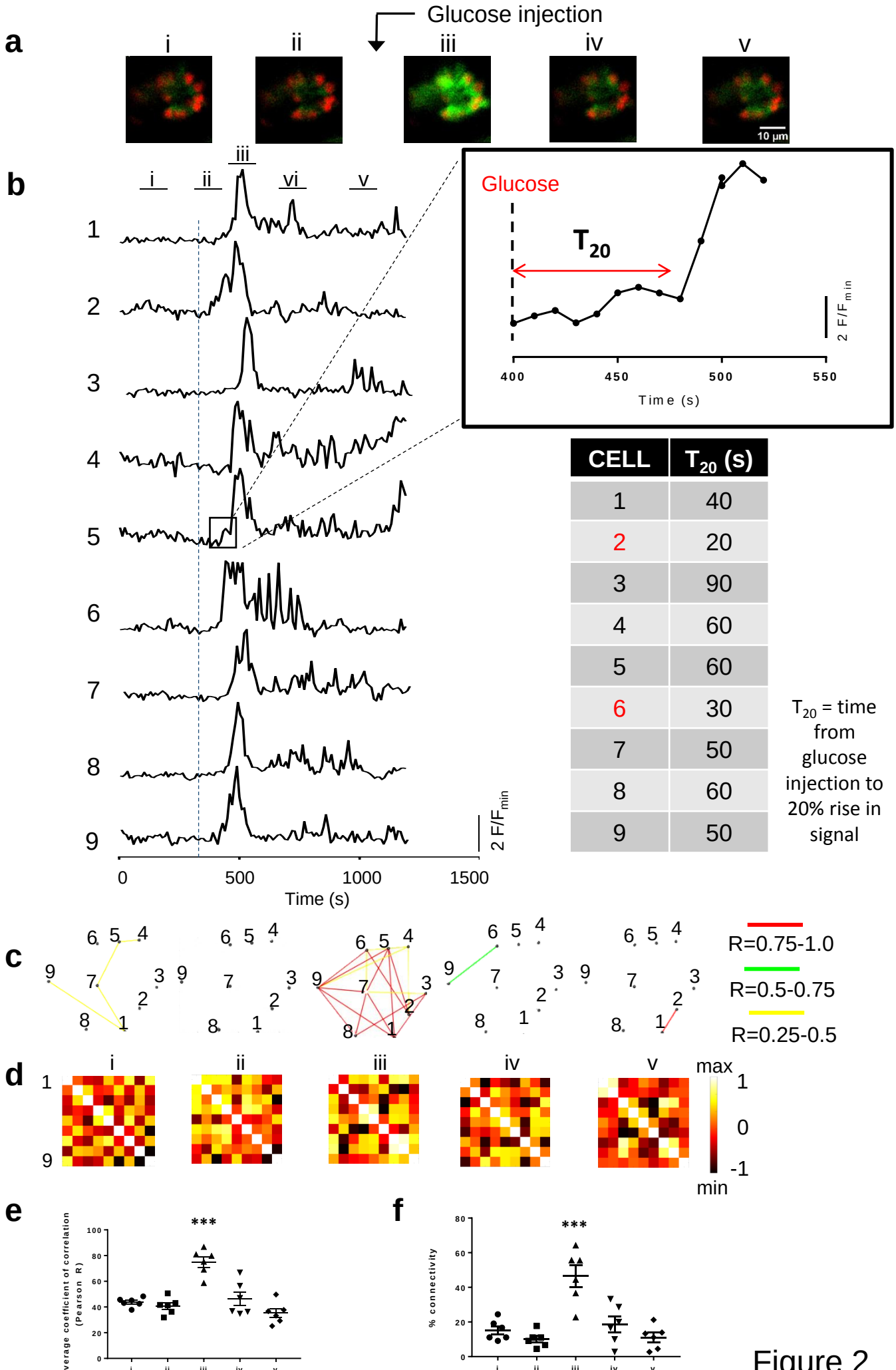

CELL	T_{20} (s)
1	40
2	20
3	90
4	60
5	60
6	30
7	50
8	60
9	50

T_{20} = time from glucose injection to 20% rise in signal

Figure 2

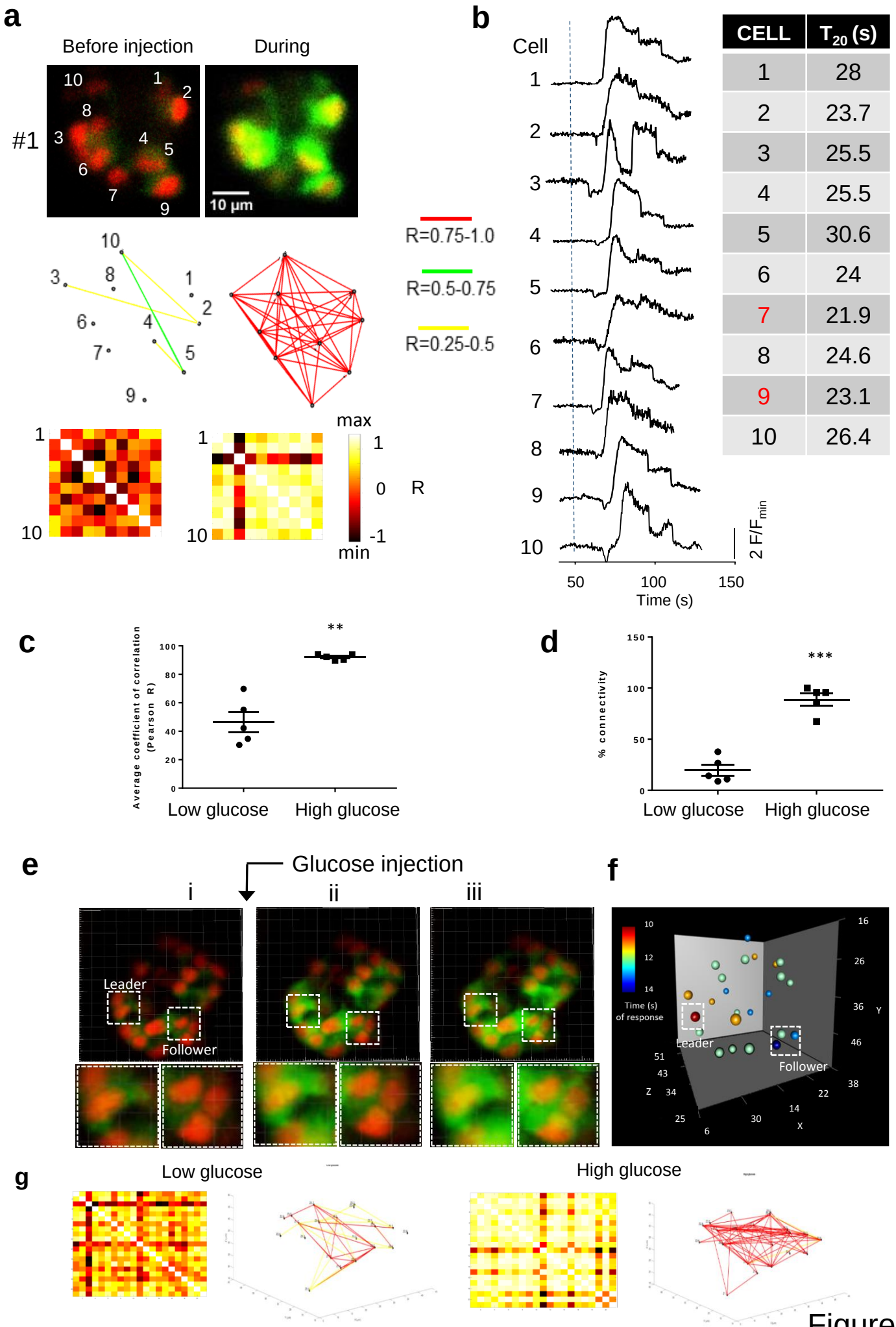

CELL	T_{20} (s)
1	28
2	23.7
3	25.5
4	25.5
5	30.6
6	24
7	21.9
8	24.6
9	23.1
10	26.4

Figure 3

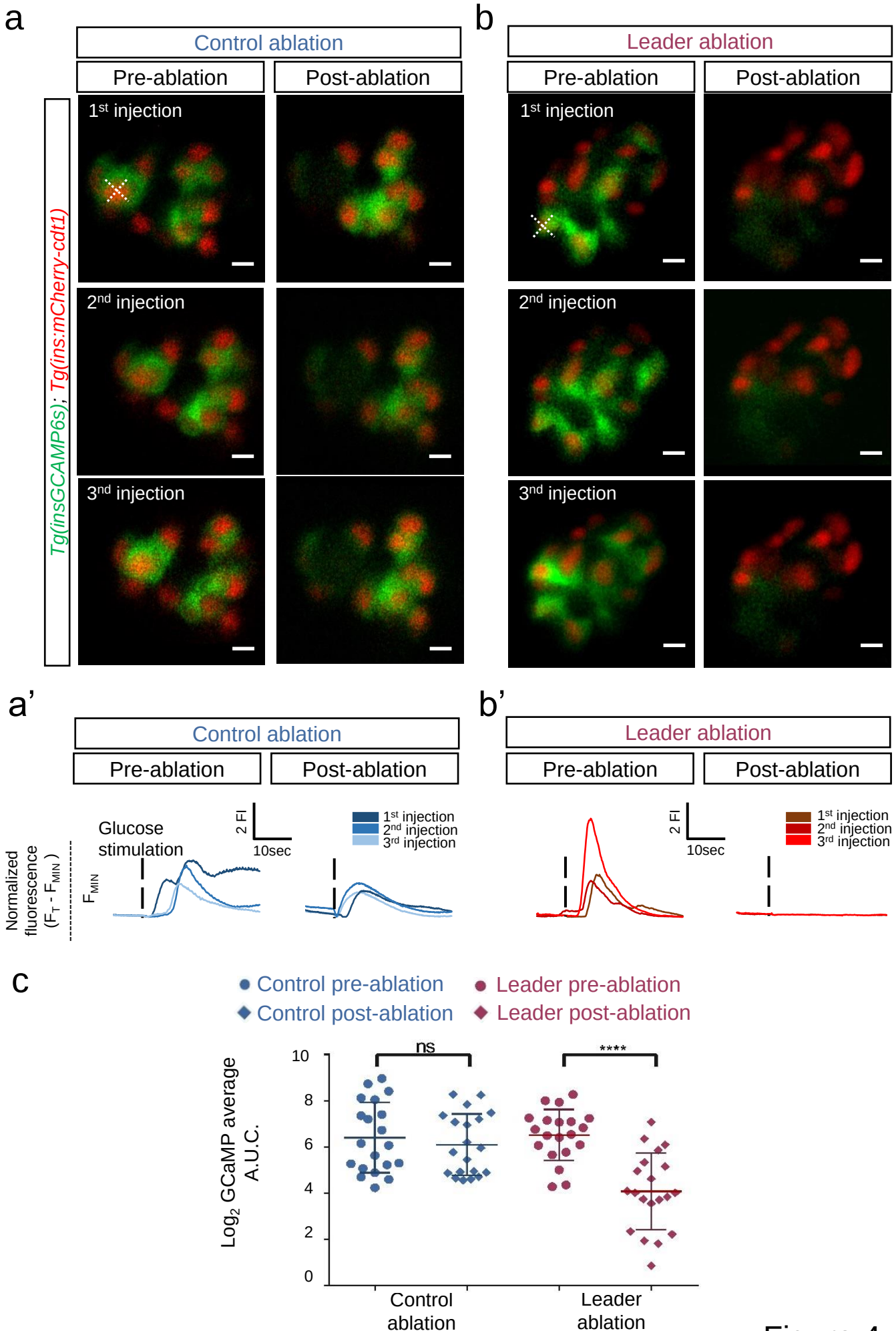
a
Control ablation
Pre-ablation
Post-ablation
Tg(insGCAMP6s); Tg(ins:mCherry-cdt1)
1st injection
2nd injection
3rd injection
b
Leader ablation
Pre-ablation
Post-ablation
1st injection
2nd injection
3rd injection
a'
Control ablation
Pre-ablation
Post-ablation
Glucose stimulation
2 FI
10sec
1st injection
2nd injection
3rd injection
Normalized fluorescence (FT - FMIN)
FMIN
b'
Leader ablation
Pre-ablation
Post-ablation
2 FI
10sec
1st injection
2nd injection
3rd injection
c
Control pre-ablation
Leader pre-ablation
Control post-ablation
Leader post-ablation
ns
****
Log2 GCaMP average A.U.C.
10
8
6
4
2
0
Control ablation
Leader ablation

Figure 4

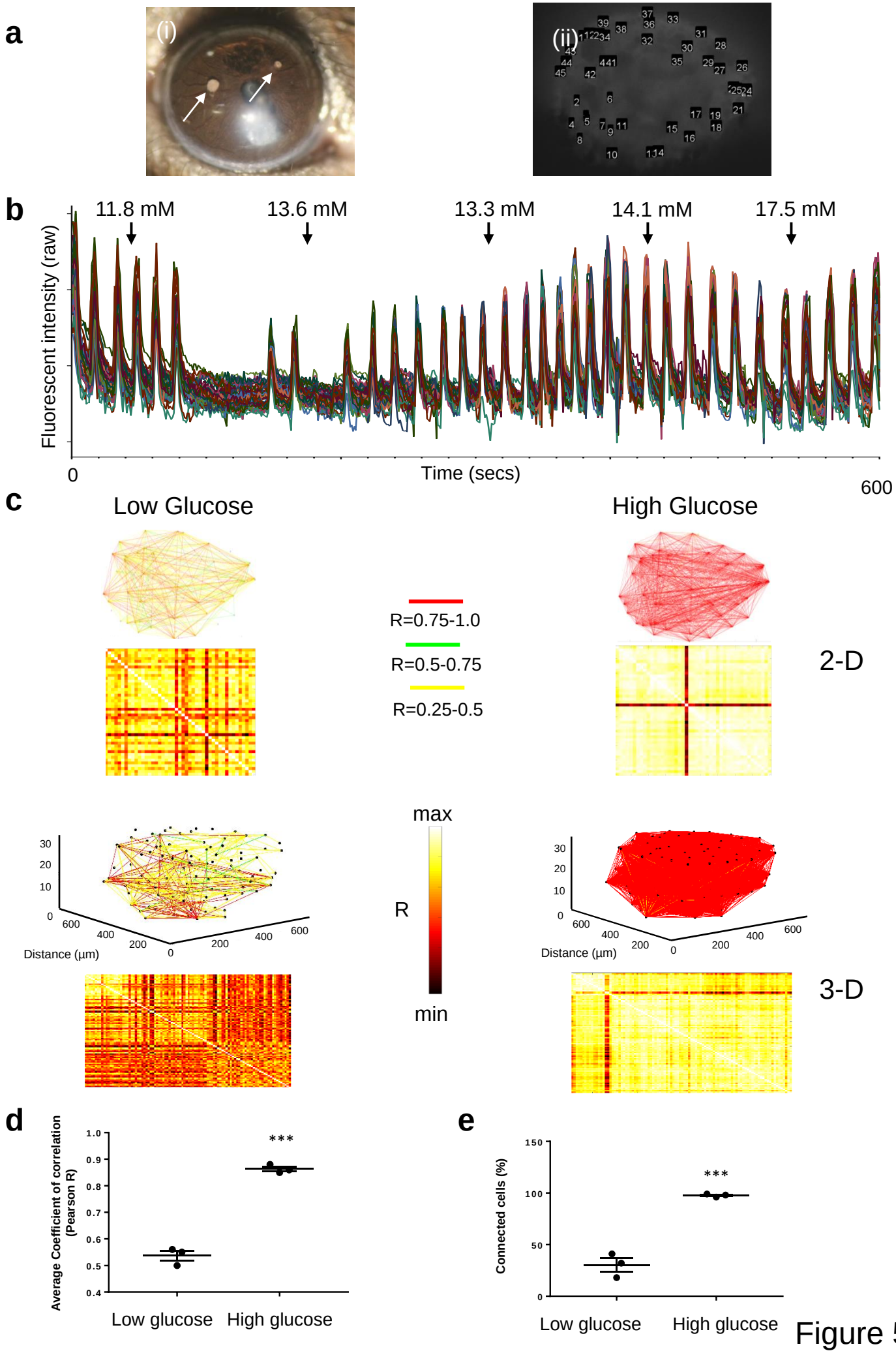
a
(i)
(ii)
b
11.8 mM
13.6 mM
13.3 mM
14.1 mM
17.5 mM
Fluorescent intensity (raw)
0
Time (secs)
600
c
Low Glucose
High Glucose
R=0.75-1.0
R=0.5-0.75
R=0.25-0.5
2-D
max
R
min
Distance (µm)
3-D
d
Average Coefficient of correlation (Pearson R)
***
Low glucose
High glucose
e
Connected cells (%)
***
Low glucose
High glucose

Figure 5

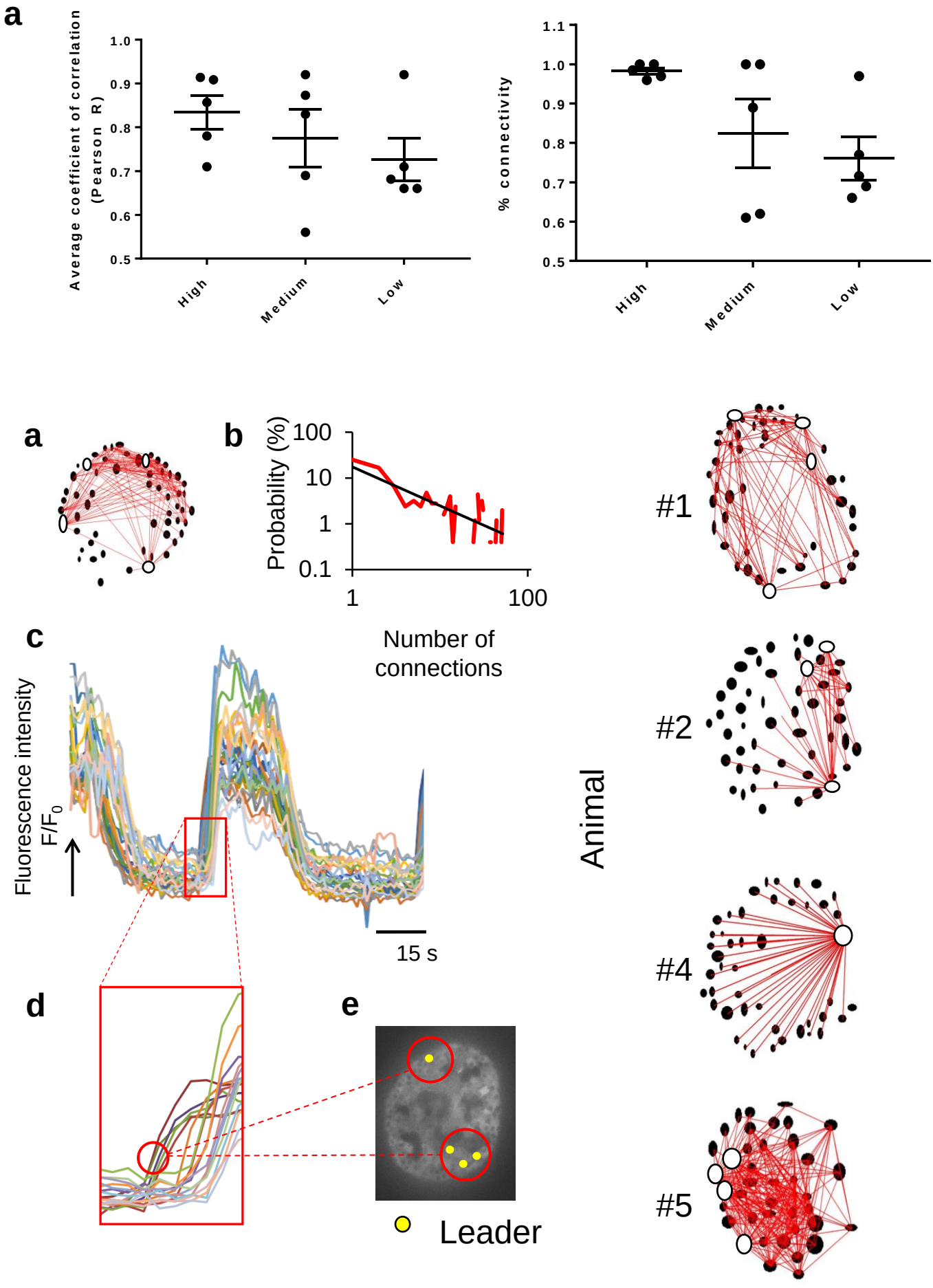
a
Average coefficient of correlation (Pearson R)
1.0
0.9
0.8
0.7
0.6
0.5
High
Medium
Low
% connectivity
1.1
1.0
0.9
0.8
0.7
0.6
0.5
High
Medium
Low
a
b
Probability (%)
100
10
1
0.1
1
100
Number of connections
#1
#2
#4
#5
Animal
c
Fluorescence intensity
F/F0
15 s
d
e
Leader

Figure 6